

OPEN ACCESS

Impedance Response of Ionic Liquids in Long Slit Pores

To cite this article: Ruben J. Tomlin *et al* 2022 *J. Electrochem. Soc.* **169** 120513

View the [article online](#) for updates and enhancements.

You may also like

- [Structural and thermodynamic properties of inhomogeneous fluids in rectangular corrugated nano-pores](#)
Yanshuang Kang, , Haijun Wang et al.

- [Fabrication of Plasmonic Nano-Slit Pore Double Layer for Single Molecule Detection](#)

Seong Soo Choi, Yong Min Lee, Byung Seong Bae et al.

- [Can ionophobic nanopores enhance the energy storage capacity of electric-double-layer capacitors containing nonaqueous electrolytes?](#)

Cheng Lian, Honglai Liu, Douglas Henderson et al.

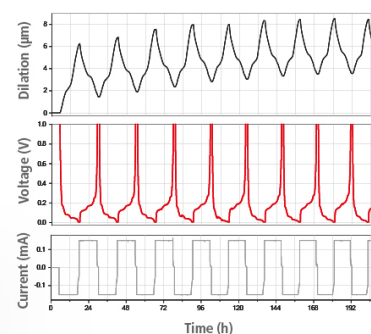
Watch Your Electrodes Breathe!

Measure the Electrode Expansion in the Nanometer Range with the ECD-4-nano.

- ✓ Battery Test Cell for Dilatometric Analysis (Expansion of Electrodes)
- ✓ Capacitive Displacement Sensor (Range 250 μm , Resolution ≤ 5 nm)
- ✓ Detect Thickness Changes of the Individual Half Cell or the Full Cell
- ✓ Additional Gas Pressure (0 to 3 bar) and Temperature Sensor (-20 to 80° C)



EL-CELL[®]
electrochemical test equipment



See Sample Test Results:



Scan me!

Download the Data Sheet (PDF):



Scan me!

Or contact us directly:

+49 40 79012-734

sales@el-cell.com

www.el-cell.com



Impedance Response of Ionic Liquids in Long Slit Pores

Ruben J. Tomlin,^{1,z} Tribeni Roy,² Toby L. Kirk,³ Monica Marinescu,¹ and Dirk Gillespie⁴

¹Department of Mechanical Engineering, Imperial College London, London SW7 2AZ, United Kingdom

²Department of Mechanical Engineering, BITS Pilani, India

³Mathematical Institute, University of Oxford, Oxford OX2 6GG, United Kingdom

⁴Department of Physiology and Biophysics, Rush University Medical Center, Chicago, IL United States of America

We study the dynamics of ionic liquids in a thin slit pore geometry. Beginning with the classical and dynamic density functional theories for systems of charged hard spheres, an asymptotic procedure leads to a simplified model which incorporates both the accurate resolution of the ion layering (perpendicular to the slit pore wall) and the ion transport in the pore length. This reduced-order model enables qualitative comparisons between different ionic liquids and electrode pore sizes at low numerical expense. We derive semi-analytical expressions for the impedance response of the reduced-order model involving numerically computable sensitivities, and obtain effective finite-space Warburg elements valid in the high and low frequency limits. Additionally, we perform time-dependent numerical simulations to recover the impedance response as a validation step. We investigate the dependence of the impedance response on system parameters and the choice of density functional theory used. The inclusion of electrostatic effects beyond mean-field qualitatively changes the dependence of the characteristic response time on the pore width. We observe peaks in the response time as a function of pore width, with height and location depending on the potential difference imposed. We discuss how the calculated dynamic properties can be used together with equilibrium results to optimise ionic liquid supercapacitors for a given application.

© 2022 The Author(s). Published on behalf of The Electrochemical Society by IOP Publishing Limited. This is an open access article distributed under the terms of the Creative Commons Attribution 4.0 License (<http://creativecommons.org/licenses/by/4.0/>), which permits unrestricted reuse of the work in any medium, provided the original work is properly cited. [DOI: 10.1149/1945-7111/ac89b5]



Manuscript submitted May 8, 2022; revised manuscript received August 9, 2022. Published December 22, 2022.

Supercapacitors are typically comprised of porous carbon-derived electrodes with an aqueous, organic, or ionic liquid electrolyte, and store charge in electrostatic double layers at all surfaces in the pore network. Models have been constructed at varying levels of complexity to describe this system and its components, i.e. individual pores, pore networks or electrodes. For short individual pores, it can be viable to perform molecular dynamics simulations to resolve the complicated many-body interactions in full, although this is often very computationally expensive. At the cell level, physics-based models have been developed with an averaging approach under the assumptions of porous electrode and dilute solution theories. These can incorporate electrolyte transport at multiple pore scales.^{1,2}

For concentrated electrolytes, such as ionic liquids, and systems where pore size and electrostatic double layer widths are comparable, Poisson–Boltzmann (PB) theory for dilute solutions becomes invalid. More complicated models have been developed, incorporating ion size (steric) effects and electrostatics beyond the mean-field description. PB theory can be modified by including steric effects in a mean-field manner,³ or by incorporating an inner layer of ions at the electrode surface (with a dilute PB outer layer) to form a composite model.⁴ Steric effects suppress the unbounded growth of the zero-frequency differential capacitance ($\partial Q/\partial V$) with voltage found in PB theory, exhibiting bell- or camel-shaped curves where either one or two maxima are present, respectively—this finding was corroborated by Kornyshev⁵ with theoretical results for a lattice-gas model, also showing that unequal ion sizes would result in the asymmetry of $\partial Q/\partial V$ about zero potential (relative to the potential in the bulk). At the level of equivalent circuit models, it can be predicted that the dynamical response time of the system (which scales linearly with the capacitance) is greatly reduced from the PB result at large voltages.⁴

Poisson–Nernst–Planck (PNP) can be modified similarly to describe the dynamical behaviours of concentrated electrolyte systems.⁶ During the charging of a parallel-plate capacitor, the double layer governed by the modified PNP system initially proceeds as it would with the unmodified PNP equations, until the packing limit is reached and the double layer extends laterally with

constant ion concentrations (while the unmodified PNP solution grows exponentially at the electrode surface). This is however a qualitatively incorrect description of how steric effects influence double layer structure.⁷ A phenomenological model with electrostatic correlations, improving on the usual mean-field electrostatics, was proposed by Bazant et al.⁸ At low voltages, overscreening/charge inversion was observed, where the magnitude of charge on the electrode surface is less than that in the first layer of counterions.

Kondrat and Kornyshev⁹ carried out a pore charging study for nanoscale slit pores using improved mean-field models with electrostatic correlations. Generally, the authors found that wider pores charged faster, and observed front-like propagation of charge into empty pores, whereas initially filled pores charged diffusively. Based on their results for single pore systems, Kondrat and Kornyshev outlined an approach for optimising porous electrode structures in which the pore widths and lengths are tuned to attain the best combination of energy and power density.

Another approach to model the behavior of confined and concentrated electrolytes is classical density functional theory (DFT). DFT computes the equilibrium behavior of inhomogeneous fluids in the presence of external potentials by minimising a free energy functional¹⁰ (the reviews of Evans¹¹ and Lutsko¹² provide an overview of the major advances in classical DFT since its inception). In DFT, ionic liquids are typically modelled as mixtures of charged hard spheres; for these systems, good approximate free energy functionals exist. The hard-sphere (steric) component is incorporated using the fundamental measure theory (FMT) derived by Rosenfeld,¹³ or the improved White Bear versions.^{14–16} Theories for electrostatic correlations, based on the mean spherical approximation (MSA) for bulk systems,¹⁷ have been derived by a number of authors.^{18–25} Both the hard-sphere and electrostatic theories used in the present work are discussed below.

Classical DFT has already been utilised extensively to analyze ionic liquid choice and pore size effects with applications in supercapacitor design. However, DFT is limited to the computation of equilibrium quantities such as the integral capacitance or $\partial Q/\partial V$. Jiang et al.²⁶ observed that the integral capacitance can have a strongly oscillatory dependence on the pore width, indicating that the optimisation of carbonaceous electrode porosities could lead to a

^zE-mail: ruben.tomlin1@imperial.ac.uk

significant increase in the energy density of an ionic liquid supercapacitor. Camel- and bell-shape plots for the differential capacitance as a function of the pore surface potential (for low and high bulk densities, respectively) have been recovered with DFT²⁷ as found in previous studies of modified PB models.^{4,5} Further work has focused on the influence of an added solvent²⁸ or other impurities,²⁹ and the possibility of mixing ionic liquids to maximise capacitance.^{30,31}

Dynamic density functional theory (DDFT) extends DFT to non-equilibrium systems.^{10,32–34} The DDFT equation has the form of a conservation law, and specifies that particle density distributions evolve according to gradients in the local chemical potentials (these are spatially varying out of equilibrium), relaxing to classical DFT equilibria. The validity of this model far from equilibrium is being investigated.³⁵ te Vrugt et al.³⁴ provide an overview of the original DDFT model of Evans¹⁰ and its extensions, with a comprehensive survey of the many applications. The DDFT system reduces to the usual diffusion equation in the case of a non-interacting ideal gas, and classical PNP can be obtained for dilute charged particle systems with a mean-field assumption for the electrostatics.

There have been a number of DDFT studies for ionic liquids, the majority of which consider a nanoscale parallel-plate capacitor set-up and focus on charging dynamics.^{36–38} Babel et al.³⁹ applied a sinusoidal voltage on the walls of the nanoscale capacitor to calculate the impedance response, performing numerical simulations both with and without mean-field electrostatics and hard-sphere effects, finding that the latter had the most significant influence on the result. For the adsorption of ionic liquids into like-charged nanoslits, authors have resorted to fixing ion densities and chemical potentials equal to bulk values on permeable pore walls, in an attempt to avoid the modelling of dynamics in the other spatial dimensions.⁴⁰ The above cited works involve spatially 1D models, and capture the fast dynamics of ionic liquids on the nanoscale.

In the present work, we are interested in using DFT and DDFT to predict the influence of the underlying ion equilibria on the impedance response. The study of impedance response of porous electrodes was pioneered by de Levie^{41–43} who modelled the system as a set of infinite and semi-infinite cylindrical pores connected in parallel. He proposed a transmission line (electrical circuit) model for the ion transport in the pores, for which the circuit parameters could be expressed in terms of physical quantities. Under a number of simplifying assumptions, including infinite electrical conductivity in the electrode (valid for carbon-based supercapacitor electrodes), the impedance response of a single semi-infinite pore homogeneously filled with electrolyte can be reduced to the finite-space Warburg (FSW) element^{44,45}

$$Z(\omega) = \mathcal{Z} \frac{\coth(\sqrt{i\omega\tau})}{\sqrt{i\omega\tau}}. \quad [1]$$

Here, $i = \sqrt{-1}$ and ω is the angular frequency of the alternating voltage/current input, \mathcal{Z} is an impedance and τ is a time constant. The high and low frequency limits of the FSW element 1 are

$$\begin{aligned} Z(\omega) &\sim \mathcal{Z} \left(\frac{1}{3} - \frac{i}{\omega\tau} \right) \quad \text{as } \omega \rightarrow 0, \\ Z(\omega) &\sim \frac{\mathcal{Z}(1-i)}{\sqrt{2\omega\tau}} \quad \text{as } \omega \rightarrow \infty, \end{aligned} \quad [2]$$

respectively.⁴⁴ The high frequency limit pertains to diffusive behavior, and at low frequencies the system is capacitive.

Analytical expressions similar to Eq. 1 can be derived if some of the assumptions used by de Levie are relaxed, as discussed in the review of Huang et al.⁴⁵ However, there has been only limited success in incorporating more complex physical models into the analytical derivations of impedance response expressions. For the planar electrode geometry, an analytical expression for the impedance response of the PNP model without the electroneutrality

assumption was derived by Li and Huang,⁴⁶ with other authors resorting to numerical investigations of modified PNP systems in the same set-up.^{47,48} Experimental works often attempt to fit data to the FSW expression 1, replacing the exponent 1/2 with an unknown (constant phase element) exponent if needed. The influence of non-trivial pore geometry was first investigated by Keiser et al.,⁴⁹ who utilised the transmission line model of de Levie and varied the circuit parameters to account for spatial dependence of the cylindrical pore radius. This problem was recently revisited by Cooper et al.⁵⁰ who performed numerical simulations of a diffusion equation in frequency space, both in open and closed pores of varying cross section and in more complicated and tortuous geometries including fractal domains. In the present work, our interest is solely in the influence of improvements to the physical model employed, keeping the geometry as simple as possible.

We study ion dynamics in idealised, spatially 2D, rectangular slit pores, for which the pore length is significantly larger than the nanoscale width. The pore is connected to an infinite particle bath, and the system is driven from equilibrium by variations of the potential on the slit walls. Due to the multi-scale nature of this problem, it would likely be intractable to solve a full 2D DDFT, let alone perform molecular dynamics simulations. We proceed with an asymptotic reduction of the DDFT system, resulting in a limit model on the timescale of supercapacitor applications for which the ion densities appear to equilibrate instantaneously in the nanoscale pore width. This model is the simplest way of incorporating both DFT, for the accurate resolution of the (out-of-plane) ion profiles, and time-dependent dynamics for the ion transport in the pore length dimension. During the preparation of this manuscript, we became aware of the work of Aslyamov et al.⁵¹ which investigates the same limit model to study slit pore charging.

We perform a frequency response analysis of the limit model, finding that it is amenable to a semi-analytical approach. We recover the FSW element 1 in the case where only one ion species is present in the pore, and construct effective FSW elements, valid in the low and high frequency limits, for the general case. Additionally, we carry out numerical simulations in which the time-dependent system is solved in response to a sinusoidal voltage input to mimic a potentiostatic electrochemical impedance spectroscopy (PEIS) experiment at the pore scale. Exploration of the system response beyond the linear PEIS regime through full numerical simulation is left to a later study, although relevant results with discontinuous voltage inputs are presented by Aslyamov et al.⁵¹ For two parameter sets inspired by real ionic liquids, we investigate the influence of system parameters and the choice of DFT. We find that the inclusion of electrostatic correlations in the DFT modify the dynamic characteristics of the pore system for widths close to those of the ions. Without electrostatic correlations, the characteristic time of the linear response appears to be overestimated for pores that can fit a single ion. We observe peaks in the response time as a function of pore width, which shift in magnitude and location depending on the base voltage. For the optimisation of supercapacitor geometries, such dynamic results should be taken together with equilibrium results to ensure that an appropriate balance of energy and power density is achieved for the desired application.

Problem Formulation and Model Reduction

We consider the dynamics of ionic liquids in slit pores of length L and width W (with an infinite third “depth” dimension) as shown in the schematic in Fig. 1. Our interest is in developing models for thin pores with $L \gg W$, where W is on the order of nanometers (comparable to typical ion sizes). The coordinates in the pore length and width are x and y , respectively, and in the following discussion we use \mathbf{r} to denote a general coordinate vector. This individual slit pore represents one of many that comprise a typical carbonaceous electrode in an electrostatic double layer capacitor, specifically of nano-wall type. The filling ionic liquid is modelled as a mixture of hard spheres with point charges located at the particle centres,

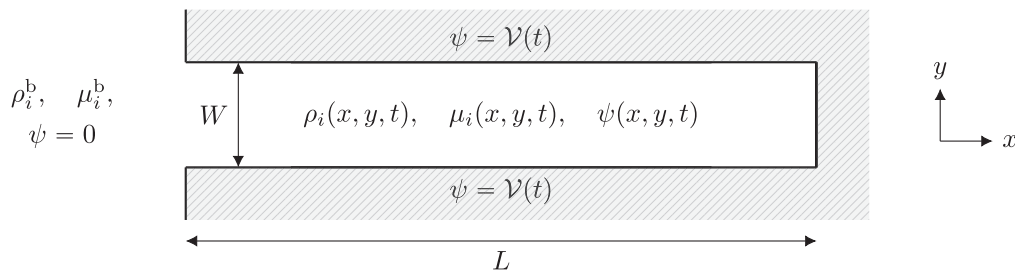


Figure 1. A single slit pore connected to an infinite particle bath.

referred to as the primitive model; specifically, the ion-ion pair potential between particles of species i, j with separation distance $r = |\mathbf{r}|$ is

$$u_{i,j}(r) = \begin{cases} \infty & \text{if } r < \sigma_i/2 + \sigma_j/2, \\ \frac{z_i z_j e^2}{4\pi\epsilon_0\epsilon_r r} & \text{if } r \geq \sigma_i/2 + \sigma_j/2, \end{cases} \quad [3]$$

where σ_i and z_i denote the diameter and valence of the i th particle species, respectively. Additionally, e is the elementary charge, ϵ_0 denotes the permittivity of free space, and ϵ_r is the dielectric constant of the medium. The electrode material is assumed to have the same dielectric constant to avoid image charges, a typical assumption in DFT studies on the pore scale. The dielectric constants of many carbonaceous electrode materials are similar to those of the ionic liquids considered here, and so the effect of a dielectric discontinuity at the pore walls is assumed to be small (its inclusion is left for future work). The electronic effects of the pore wall are neglected in this work, although they have recently been incorporated into a unifying functional theory by Huang et al.⁵²

The time evolution of the ion density distributions in the pore, denoted $\rho_i(\mathbf{r}, t)$, are governed by the deterministic DDFT system first written down by Evans,¹⁰

$$\frac{\partial \rho_i}{\partial t} = \beta D_i \nabla \cdot (\rho_i \nabla \mu_i). \quad [4]$$

Here, μ_i are the local chemical potentials, which are spatially varying out of equilibrium. Gradients in the local chemical potentials drive the density evolution, and without external forcing, solutions of Eq. 4 relax to equilibrium DFT solutions with constant μ_i . The product βD_i is the mobility of the i th species, where D_i denotes a single-particle self-diffusion coefficient and $\beta = 1/k_B T$ is the thermodynamic inverse temperature (both β and the D_i are assumed constant in this work). At the pore cap we impose a no-flux boundary condition, $\partial_x \mu_i = 0$ at $x = L$, as well as on the long sides of the slit pore, $\partial_y \mu_i = 0$ at $y = 0, W$. At $x = 0$, the pore is open and connected to an infinite particle bath, with bulk densities and chemical potentials in the far field denoted by ρ_i^b and μ_i^b , respectively. When the system is at rest, the chemical potentials in the pore equal those in the bulk, $\mu_i = \mu_i^b$. The relationship between the densities and local chemical potentials, required to close the system, is based on that used in classical DFT for particle systems in equilibrium, as described next.

The pair interaction potential 3 uniquely determines an intrinsic Helmholtz free energy, $F[\{\rho_i\}]$, a functional of the particle densities.¹⁰ This free energy is independent of the external potentials, denoted U_i , which describe the influence of the pore walls on each ion species. The grand potential energy density functional for the system is given by

$$\Omega[\{\rho_i\}] = F[\{\rho_i\}] + \sum_i \int (U_i - \mu_i) \rho_i \, d\mathbf{r}. \quad [5]$$

Equilibrium DFT solutions are obtained as minimisers of Ω , satisfying the Euler–Lagrange equation,

$$0 = \frac{\delta \Omega}{\delta \rho_i} = \frac{\delta F}{\delta \rho_i} + U_i - \mu_i, \quad [6]$$

which is also used to relate the constant bulk quantities ρ_i^b and μ_i^b (for which $U_i = 0$). The DDFT assumption is that Eq. 6 remains valid close to equilibrium, and so yields the desired expression for the local chemical potentials to be used in Eq. 4. While there exists a unique Helmholtz free energy corresponding to the particle interactions 3, it cannot be written down exactly (analytical expressions for F only exist for special cases of $u_{i,j}$). For an exact Helmholtz free energy, it can be shown that there is a unique correspondence between the external potential and the equilibrium density,¹⁰ as the minimisation problem is convex, yielding a unique global minimum (unique equilibrium). The DFT approach relies critically on the ability to construct accurate approximations of F . However, the convexity property of the minimisation problem can be lost during this approximation process, and sometimes more than one equilibrium solution exists for a given external potential with an approximate free energy.³⁴

Typically, F is decomposed into ideal and excess components, and for the case of pair potential 3, the excess free energy is split up into contributions due to hard-sphere and electrostatic interactions, with the latter broken down further into mean-field direct Coulomb interactions and electrostatic correlations (sometimes referred to as the electrostatic residual or screening contribution),

$$F = F^{\text{ID}} + F^{\text{EX}} = F^{\text{ID}} + F^{\text{HS}} + F^{\text{CO}} + F^{\text{EC}}. \quad [7]$$

The ideal component corresponds to the intrinsic Helmholtz free energy for a system of noninteracting particles, i.e. $u_{i,j} \equiv 0$, and is given exactly by

$$F^{\text{ID}}[\{\rho_i\}] = \beta^{-1} \sum_i \int (\log(\Lambda_i^3 \rho_i(\mathbf{r})) - 1) \rho_i(\mathbf{r}) \, d\mathbf{r}, \quad [8]$$

where Λ_i is an effective (de Broglie) thermal wavelength.⁵³ If F^{EX} , $U_i = 0$, the local chemical potential is given by $\mu_i = \beta^{-1} \log \rho_i$ and returns the standard diffusion equation when substituted into Eq. 4. Substituting Eqs. 7, 8 into the Euler–Lagrange equation 6 gives

$$\rho_i(\mathbf{r}) = \Lambda_i^{-3} \exp \left[-\beta \left(\frac{\delta F^{\text{EX}}}{\delta \rho_i} + U_i(\mathbf{r}) - \mu_i \right) \right]. \quad [9]$$

This implicit expression for the densities is commonly used as the basis of Picard iteration numerical schemes for equilibrium DFT calculations. The Λ_i can be absorbed into the chemical potentials or, at equilibrium, can be cancelled by relating the bulk densities and chemical potentials.⁵⁴

The direct Coulomb contribution to the excess free energy is

$$F^{\text{CO}} = \frac{1}{2} \frac{e^2}{4\pi\epsilon_0\epsilon_r} \sum_{i,j} \iint \frac{z_i z_j \rho_i(\mathbf{r}) \rho_j(\mathbf{r}')}{|\mathbf{r} - \mathbf{r}'|} \, d\mathbf{r}' \, d\mathbf{r}. \quad [10]$$

This is the leading order term of the expansion of the excess free energy functional corresponding to the pair interaction $u_{ij}(r) = e^2 z_i z_j / 4\pi \epsilon_0 \epsilon_r r$, and comprises the electrostatics employed in the PB theory valid for weak electrolytes. This mean-field expression treats the particles as fully uncorrelated, only accounting for the potential created on a given particle by the mean particle distribution.^{11,53} The external potential we consider can be decomposed into the sum of hard-wall and electrostatic components, $U_i = U_i^{\text{HW}} + U_i^{\text{ES}}$, where U_i^{ES} can be identified as the electrostatic potential energy of an ion of charge ez_i in the presence of the electrostatic potential generated by all non-ionic charges in the system (e.g. charged walls). The mean electrostatic potential $\psi(\mathbf{r})$, incorporating the electrostatic components due to ionic and non-ionic charges,^{55–57} is defined by

$$\begin{aligned} ez_i \psi(\mathbf{r}) &= \frac{\delta F^{\text{CO}}}{\delta \rho_i} + U_i^{\text{ES}}(\mathbf{r}) \\ &= ez_i \sum_j \int \frac{ez_j \rho_j(\mathbf{r}')}{4\pi \epsilon_0 \epsilon_r |\mathbf{r} - \mathbf{r}'|} d\mathbf{r}' + U_i^{\text{ES}}(\mathbf{r}). \end{aligned} \quad [11]$$

The electrostatic potential satisfies the Poisson equation in the ionic liquid phase (the non-ionic component is harmonic in this region),

$$\epsilon_0 \epsilon_r \nabla^2 \psi = -e \sum_i z_i \rho_i. \quad [12]$$

As indicated in Fig. 1, we impose a voltage (measured relative to zero potential in the bulk) at the pore walls,

$$\psi|_{y=0} = \psi|_{y=W} = \mathcal{V}(t), \quad [13]$$

which we use to drive the system from equilibrium. Without contributions to the free energy from hard-sphere effects and electrostatic correlations, the local chemical potential becomes $\mu_i = \beta^{-1} \log \rho_i + ez_i \psi$. This recovers the Nernst–Planck equation when substituted into Eq. 4.

For the hard-sphere component, F^{HS} , we use the White Bear II functional developed by Hansen-Goos and Roth,¹⁶ improving on Rosenfeld's original FMT functional.¹³ We also performed computations with FMT and White Bear I,^{14,15} finding that the influence of this choice was negligible. Further discussion of the various hard-sphere functionals can be found in the review by Roth.⁵⁸

The earliest approximation of the electrostatic correlation contribution was derived independently by Kierlik and Rosinberg²¹ and Rosenfeld.²² They used functional Taylor expansions about constant bulk densities with coefficients (direct correlation functions) given by the MSA. This bulk fluid density (BFD) approach was refined by Gillespie et al.^{23,24} using self-consistent non-homogeneous reference densities in the Taylor expansion, termed reference fluid density (RFD) theory, with the resulting equilibrium profiles often in close agreement to molecular simulations.⁵⁹ More recently, functionalised mean spherical approximation (fMSA) was developed by Roth and Gillespie²⁵ which significantly reduces the computational complexity with only some loss of accuracy (compared to RFD).⁵⁹ In the present work, we show results for both BFD and fMSA theories. In their study of pore charging, Aslyamov et al.⁵¹ use FMT and the weighted correlation approach (for F^{EC}) developed by Wang et al.,⁵⁵ the accuracy of which has not been systematically investigated.

The formulation of the grand potential energy density functional 5 is completed with the hard-wall component of the external potential, which away from the pore extremities is a function of y alone,

$$U_i^{\text{HW}}(y) = \begin{cases} 0 & \text{if } \sigma_i/2 \leq y \leq W - \sigma_i/2, \\ \infty & \text{otherwise.} \end{cases} \quad [14]$$

This enforces non-overlapping of the pore wall and the spherical ions, with the density profiles of the latter dropping to zero within one radius of the wall.

Asymptotic model reduction.—We consider the DDFT Eq. 4 in 2D from here onwards, assuming uniform densities in the infinite depth dimension. The focus of the present work is the case of thin slit pores, for which we introduce a scale separation parameter $\epsilon = W/L \ll 1$. Additionally, we are only concerned with dynamics on the timescales of supercapacitor applications (with typical frequencies ranging from 0.001 to 1000 Hz) which are significantly longer than the nanosecond diffusion times of ionic liquids (see parameter sets below). Since a full asymptotic derivation of the model valid in the limit as $\epsilon \rightarrow 0$ has already been presented by Aslyamov et al.,⁵¹ we provide an informal derivation following discussions for the related problem of anisotropic diffusion equations.^{60,61}

With the auxiliary pore length variable $x^* = \epsilon x$ and slow time-scale $t^* = \epsilon^2 t$, we obtain the rescaled DDFT equation

$$\frac{\partial \rho_i}{\partial t^*} = \beta D_i \frac{\partial}{\partial x^*} \left(\rho_i \frac{\partial \mu_i}{\partial x^*} \right) + \frac{1}{\epsilon^2} \beta D_i \frac{\partial}{\partial y} \left(\rho_i \frac{\partial \mu_i}{\partial y} \right), \quad [15]$$

where, in (x^*, y) coordinates, the pore is a square of side W . Since we do not wish to resolve the dynamics on the fast timescale, we may formally set $\epsilon = 0$ in the above equation to obtain

$$0 = \beta D_i \frac{\partial}{\partial y} \left(\rho_i \frac{\partial \mu_i}{\partial y} \right). \quad [16]$$

This is equivalent to the statement that, to leading order, the densities locally satisfy a 1D equilibrium DFT system in the pore width defined by the Euler–Lagrange equation 6 with uniform in y , yet undetermined, chemical potentials $\mu_i \equiv \mu_i(x, t)$. It is important to note that, while the ion densities satisfy an equilibrium problem, they are not necessarily *in equilibrium* with the bulk phase external to the pore.

Equation 16 is a constraint that neither fully specifies an equilibrium problem at each x nor informs the time-evolution of the system; to provide the correct well-posed limit model it must be allied with the appropriate integral equation.⁶¹ The latter is obtained by integrating the DDFT equation in y and applying the no-flux boundary conditions, annihilating the final term in Eq. 15 for any ϵ . In (x, t) variables, we arrive at

$$\frac{\partial N_i}{\partial t} = \beta D_i \frac{\partial}{\partial x} \left(\int_0^W \rho_i \frac{\partial \mu_i}{\partial x} dy \right), \quad [17]$$

where we define the particle numbers (per unit of pore length and depth)

$$N_i(x, t) = \int_0^W \rho_i(x, y, t) dy. \quad [18]$$

Taking the limit $\epsilon \rightarrow 0$, we may use the fact that the μ_i are independent of y , and the integral equation becomes

$$\frac{\partial N_i}{\partial t} = \beta D_i \frac{\partial}{\partial x} \left(N_i \frac{\partial \mu_i}{\partial x} \right). \quad [19]$$

Equation 19 describes the evolution of the particle numbers and is the same as the limit equation derived by Aslyamov et al.,⁵¹ who expressed theirs in terms of the width-averaged densities, $\bar{\rho}_i = N_i/W$. Accordingly, we solve a canonical 1D equilibrium problem at each x for the ion densities as a function of y , where the particle numbers 18 are prescribed. This is as opposed to solving a grand canonical problem where the chemical potentials are given. The numerical approach is discussed in Appendix A.1. As an output of this equilibrium problem, we obtain the chemical potentials μ_i at each x , gradients of which are required to evolve the particle numbers in time according to Eq. 19. There exist DFTs specifically for canonical calculations with a small integer number of particles,⁶²

e.g. hard spheres in a closed cavity. However, since our slit pore extends infinitely in the direction perpendicular to the x - y plane, we can perform a thermodynamic limit, and use DFTs derived originally in the grand canonical framework with the additional particle number constraint 18.

The 3D DFT components discussed above must be restricted to a planar 1D geometry for use in the canonical equilibrium problem. The 1D weight functions for the hard-sphere terms are given by Roth,⁵⁸ while the expressions for the correlations according to the BFD and fMSA theories are provided by Gillespie et al.,²³ and Roth and Gillespie,²⁵ respectively. For the electrostatics, the left hand side of the Poisson equation 12 becomes $\epsilon_0 \epsilon_r \psi_{yy}$. Using Gauss' law, we can compute the surface charge density along the long pore walls as a function of time,

$$\psi_y|_{y=0} = -\frac{Q_0(x, t)}{\epsilon_0 \epsilon_r}, \quad \psi_y|_{y=W} = +\frac{Q_W(x, t)}{\epsilon_0 \epsilon_r}. \quad [20]$$

Integrating the Poisson equation 12 over the full pore width, $y \in [0, W]$, and applying the Neumann conditions 20 gives the instantaneous charge neutrality expression for a fixed- x slice of the pore,

$$Q = Q_0 + Q_W = -e \sum_i z_i N_i, \quad [21]$$

where $Q(x, t)$ denotes the sum of the local surface charge densities on the pore walls. When the entire system is at equilibrium, the chemical potentials in the pore equal those in the bulk and Q is independent of x and t . We can use Eq. 21 to compute the zero-frequency differential capacitance, $\partial Q / \partial \mathcal{V}$ (denoting the rate of change of Q in \mathcal{V} for fixed μ_i), and the integral capacitance, $Q / (\mathcal{V} - \mathcal{V}_{zc})$, where \mathcal{V}_{zc} is the potential of zero charge (i.e. $Q(\mathcal{V}_{zc}) = 0$).

At the pore entrance and cap, the asymptotics break down and spatially 2D density profiles are expected; the full resolution of these regions is beyond the scope of the present study. Instead, at the entrance we fix the chemical potentials equal to those in the bulk,

$$\mu_i = \mu_i^b \quad \text{at } x = 0. \quad [22]$$

The particle numbers at $x=0$ are then computed from solving the grand canonical problem for 1D DFT equilibria (these will be time-dependent as the surface potential varies). At the pore cap, we ignore electrostatic effects due to the charged bounding wall and simply enforce a no-flux condition,

$$\frac{\partial \mu_i}{\partial x} = 0 \quad \text{at } x = L. \quad [23]$$

Impedance Response Analysis

Semi-analytical approach.—Following a similar route to that outlined by Huang et al.,⁴⁵ we construct an expression for the frequency response of the limit model which incorporates numerically computable sensitivities. The base state for the following linear analysis is a pore at equilibrium with the bulk phase ($\mu_i = \mu_i^b$), for which the equilibrium particle numbers are \bar{N}_i (at all values of x) given a potential $\bar{\mathcal{V}}$ applied on the pore walls. While the above theory is valid for general many-component mixtures of ionic liquids, we study two-component ionic liquids exclusively in this work. Variables and constants corresponding to the cation are indicated with a subscript +, while anion quantities have a subscript -.

To mimic a potentiostatic impedance response experiment at the pore scale, we prescribe a voltage of the form $\mathcal{V}(t) = \bar{\mathcal{V}} + \Delta \mathcal{V}(t)$, where we use Δ to denote perturbation variables which we assume to be small. Writing $\mu_i \equiv \mu_i(N_+, N_-, \mathcal{V})$, the chemical potential in the

slit has the Taylor expansion up to linear order in the perturbation variables,

$$\mu_i \approx \mu_i^b + \frac{\partial \mu_i}{\partial N_+} \Delta N_+ + \frac{\partial \mu_i}{\partial N_-} \Delta N_- + \frac{\partial \mu_i}{\partial \mathcal{V}} \Delta \mathcal{V}, \quad [24]$$

where the partial derivatives are evaluated at the base state. Since shifting the voltage on the pore walls with fixed particle numbers simply results in a corresponding shift in \mathcal{V} with the equilibrium densities unchanged, and with Eqs. 6, 11, we have $\partial \mu_i / \partial \mathcal{V} = e z_i$. The sensitivities with respect to the particle numbers must be computed numerically in general (these are calculated by solving the canonical equilibrium problem, as discussed in Appendix A.1, with perturbed particle numbers). The linearisation of Eq. 19 about the equilibrium state is

$$\frac{\partial \Delta N_i}{\partial t} = \beta D_i \bar{N}_i \frac{\partial^2}{\partial x^2} \left(\frac{\partial \mu_i}{\partial N_+} \Delta N_+ + \frac{\partial \mu_i}{\partial N_-} \Delta N_- \right), \quad [25]$$

with the boundary condition at the pore entrance, from 22,

$$\frac{\partial \mu_i}{\partial N_+} \Delta N_+ + \frac{\partial \mu_i}{\partial N_-} \Delta N_- = -e z_i \Delta \mathcal{V} \quad \text{at } x = 0, \quad [26]$$

and the no-flux condition at the pore cap, from 23,

$$\frac{\partial}{\partial x} \left(\frac{\partial \mu_i}{\partial N_+} \Delta N_+ + \frac{\partial \mu_i}{\partial N_-} \Delta N_- \right) = 0 \quad \text{at } x = L. \quad [27]$$

With the solution of the above system and using Eq. 21, the perturbation to the local surface charge density, a function of x and t , is calculated as

$$\Delta Q = -e z_+ \Delta N_+ - e z_- \Delta N_-. \quad [28]$$

Taking Fourier transforms of the perturbation variables in time, defined as

$$\Delta \hat{\mathcal{V}}(\omega) = \int_{-\infty}^{\infty} \Delta \mathcal{V}(t) e^{-i\omega t} dt, \quad [29]$$

we form the complex impedance per unit of pore depth and length (with units $\Omega \text{ m}^2$),

$$Z = \Delta \hat{\mathcal{V}} \left(\frac{i\omega}{L} \int_0^L \Delta \hat{Q} dx \right)^{-1}, \quad [30]$$

where $\omega = 2\pi f$ is the angular frequency for a temporal frequency f (Hz). The bracketed term in the impedance expression 30 is the Fourier transform of a current perturbation (averaged in the pore length dimension). From the complex impedance, we may obtain the frequency-dependent differential capacitance (in F m^{-2}) defined by

$$C_{\text{diff}} = \frac{-1}{\omega \text{Im}[Z]}. \quad [31]$$

The use of the average charge perturbation as opposed to the total charge perturbation in 30 is so that the differential capacitance 31 is comparable with results for spatially 1D studies of slit pores, with the property that

$$C_{\text{diff}} \rightarrow \frac{\partial Q}{\partial \mathcal{V}} \quad \text{as } \omega \rightarrow 0. \quad [32]$$

Single species case.—If one of the ion species is not present in the pore, Eqs. 25, 26, 27 for the perturbations are significantly reduced. For example, if $W < \sigma_+$, we have $\bar{N}_+ = 0$ and it can be surmised that $\Delta N_+ = 0$. The problem that remains for ΔN_- is

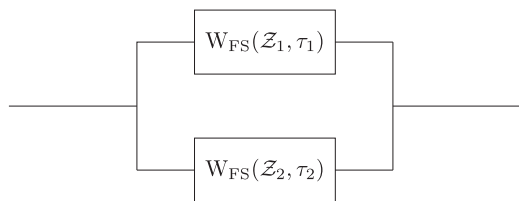


Figure 2. Circuit element interpretation of the linear impedance 44 of the slit pore. Here, $W_{FS}(Z, \tau)$ denotes a finite-space Warburg element with impedance defined by 1.

$$\frac{\partial \Delta N_-}{\partial t} = \beta D_- \bar{N}_- \frac{\partial \mu_-}{\partial N_-} \frac{\partial^2 \Delta N_-}{\partial x^2}, \quad [33]$$

with

$$\begin{aligned} \frac{\partial \mu_-}{\partial N_-} \Delta N_- &= -e z_- \Delta \mathcal{V} \quad \text{at } x = 0, \\ \frac{\partial \Delta N_-}{\partial x} &= 0 \quad \text{at } x = L. \end{aligned} \quad [34]$$

In frequency space, the solution is given by

$$\begin{aligned} \Delta \hat{N}_- &= \frac{\tau}{Z e z_-} [\tanh(\sqrt{i\omega\tau}) \sinh(\sqrt{i\omega\tau} x/L) \\ &\quad - \cosh(\sqrt{i\omega\tau} x/L)] \Delta \hat{\mathcal{V}}, \end{aligned} \quad [35]$$

where

$$Z = \frac{L^2}{e^2 z_-^2 \beta D_- \bar{N}_-}, \quad \tau = \frac{L^2}{\beta D_- \bar{N}_- (\partial \mu_- / \partial N_-)}. \quad [36]$$

With the substitution of 35 and $\Delta \hat{Q} = -e z_- \Delta \hat{N}_-$ into the complex impedance expression 30, we obtain precisely the FSW impedance 1 with parameters 36. The above time constant is a rescaling of the diffusive time constant L^2/D_- by a non-dimensional factor which incorporates the complicated DFT description of the confined ions.

Using the zero frequency limit of the FSW element from 2 with Eqs. 31, 32, 36 gives

$$\frac{\partial Q}{\partial \mathcal{V}} = \frac{\tau}{Z} = \frac{e^2 z_-^2}{\partial \mu_- / \partial N_-}. \quad [37]$$

This relation can also be obtained from $Q = -e z_- N_-$ and the cyclic chain rule for partial derivatives.

General case.—In the situation that both ion species are present in the pore, we again take a Fourier transform in time of Eqs. 25, 26, 27 and work with the new variables

$$\hat{A}_i = \frac{\partial \mu_i}{\partial N_+} \Delta \hat{N}_+ + \frac{\partial \mu_i}{\partial N_-} \Delta \hat{N}_- \quad \text{for } i = +, -, \quad [38]$$

with which we can write the system in the form

$$\begin{aligned} \frac{\partial^2 \hat{A}}{\partial x^2} &= \frac{i\omega}{\beta} M \hat{A}, \\ \hat{A}_i &= -e z_i \Delta \hat{\mathcal{V}} \quad \text{at } x = 0, \\ \frac{\partial \hat{A}}{\partial x} &= \mathbf{0} \quad \text{at } x = L, \end{aligned} \quad [39]$$

where the matrix M is

$$\begin{aligned} M &= \frac{1}{|J|} \begin{pmatrix} (\partial \mu_- / \partial N_-) / D_+ \bar{N}_+ & -(\partial \mu_+ / \partial N_-) / D_+ \bar{N}_+ \\ -(\partial \mu_- / \partial N_+) / D_- \bar{N}_- & (\partial \mu_+ / \partial N_+) / D_- \bar{N}_- \end{pmatrix}, \\ |J| &= \frac{\partial \mu_+}{\partial N_+} \frac{\partial \mu_-}{\partial N_-} - \frac{\partial \mu_+}{\partial N_-} \frac{\partial \mu_-}{\partial N_+}. \end{aligned} \quad [40]$$

If λ_1 and λ_2 denote the eigenvalues of M , corresponding to eigenvectors $\mathbf{v}_1 = (v_1, 1)^T$ and $\mathbf{v}_2 = (v_2, 1)^T$, respectively, the solution to this system is

$$\begin{aligned} \frac{\hat{A}_+}{e \Delta \hat{\mathcal{V}}} &= v_1 a_1 [\tanh(\sqrt{i\omega \lambda_1 / \beta} L) \sinh(\sqrt{i\omega \lambda_1 / \beta} x) \\ &\quad - \cosh(\sqrt{i\omega \lambda_1 / \beta} x)] \\ &\quad + v_2 a_2 [\tanh(\sqrt{i\omega \lambda_2 / \beta} L) \sinh(\sqrt{i\omega \lambda_2 / \beta} x) \\ &\quad - \cosh(\sqrt{i\omega \lambda_2 / \beta} x)], \end{aligned} \quad [41]$$

$$\begin{aligned} \frac{\hat{A}_-}{e \Delta \hat{\mathcal{V}}} &= a_1 [\tanh(\sqrt{i\omega \lambda_1 / \beta} L) \sinh(\sqrt{i\omega \lambda_1 / \beta} x) \\ &\quad - \cosh(\sqrt{i\omega \lambda_1 / \beta} x)] \\ &\quad + a_2 [\tanh(\sqrt{i\omega \lambda_2 / \beta} L) \sinh(\sqrt{i\omega \lambda_2 / \beta} x) \\ &\quad - \cosh(\sqrt{i\omega \lambda_2 / \beta} x)], \end{aligned} \quad [42]$$

where $(a_1, a_2)^T$ satisfies

$$\begin{pmatrix} v_1 & v_2 \\ 1 & 1 \end{pmatrix} \begin{pmatrix} a_1 \\ a_2 \end{pmatrix} = \begin{pmatrix} z_+ \\ z_- \end{pmatrix}. \quad [43]$$

Defining time constants $\tau_j = L^2 \lambda_j / \beta$ for $j = 1, 2$, the complex impedance 30 can be expressed as

$$\begin{aligned} \frac{L^2}{e^2 \beta} Z^{-1} &= z_+ D_+ \bar{N}_+ [v_1 a_1 \sqrt{i\omega \tau_1} \tanh(\sqrt{i\omega \tau_1}) \\ &\quad + v_2 a_2 \sqrt{i\omega \tau_2} \tanh(\sqrt{i\omega \tau_2})] \\ &\quad + z_- D_- \bar{N}_- [a_1 \sqrt{i\omega \tau_1} \tanh(\sqrt{i\omega \tau_1}) \\ &\quad + a_2 \sqrt{i\omega \tau_2} \tanh(\sqrt{i\omega \tau_2})]. \end{aligned} \quad [44]$$

The above complex impedance can be expressed as the harmonic mean of the complex impedances of two FSW elements 1, with impedance parameters

$$\begin{aligned} Z_1^{-1} &= \frac{e^2 \beta a_1}{L^2} (z_+ D_+ \bar{N}_+ v_1 + z_- D_- \bar{N}_-), \\ Z_2^{-1} &= \frac{e^2 \beta a_2}{L^2} (z_+ D_+ \bar{N}_+ v_2 + z_- D_- \bar{N}_-), \end{aligned} \quad [45]$$

and time constants τ_1 and τ_2 , respectively. In other words, the linear dynamics of the slit pore can be effectively represented by two FSW elements in parallel, as shown in Fig. 2. The time constants, incorporating both the confinement and coupling of the ionic system, generally cannot be separated into distinct physical processes. Two distinct timescales were found by Henrique et al.⁶³ for the simpler

Table I. Physical parameters based on [EMIm][TFSI] and [EMIm][BF₄].

Ionic liquid	I—[EMIm][TFSI]	II—[EMIm][BF ₄]
ϵ_r	12	14.5
σ_+ (nm)	0.5	0.5
σ_- (nm)	0.5	0.3
D_+ ($\times 10^{-11}$ m ² s ⁻¹)	6.746	5.322
D_- ($\times 10^{-11}$ m ² s ⁻¹)	3.771	4.461
σ_+^2/D_+ (ns)	3.706	4.698

PNP model in a cylindrical pore, for which it can be shown that the time constants reduce to the individual diffusion times for the constituent ions (L^2/D_{\pm}) in the limit of overlapping double layers.

For small frequencies, the complex impedance behaves according to

$$\begin{aligned} \frac{L^2}{e^2\beta} Z^{-1} \sim & \frac{\omega^2}{3} (z_+ D_+ \bar{N}_+ [v_1 a_1 \tau_1^2 + v_2 a_2 \tau_2^2] \\ & + z_- D_- \bar{N}_- [a_1 \tau_1^2 + a_2 \tau_2^2]) \\ & + i\omega (z_+ D_+ \bar{N}_+ [v_1 a_1 \tau_1 + v_2 a_2 \tau_2] \\ & + z_- D_- \bar{N}_- [a_1 \tau_1 + a_2 \tau_2]) \quad \text{as } \omega \rightarrow 0. \end{aligned} \quad [46]$$

The asymptotic behavior 46 fully prescribes an “effective” FSW element 1, valid for small frequencies, with parameters denoted Z_0 and τ_0 ; these are found by substituting $Z^{-1} \approx Z_0^{-1}(i\omega\tau_0 + \omega^2\tau_0^2/3)$ into 46. The zero frequency limit 46 can also be used to compute a relation between the chemical potential sensitivities and $\partial Q/\partial V$, although more convoluted than 37, and we may also obtain the asymptote of $\text{Re}[Z]$,

$$\begin{aligned} \frac{3e^2\beta}{L^2} \text{Re}[Z] \rightarrow & \frac{z_+ D_+ \bar{N}_+ [v_1 a_1 \tau_1^2 + v_2 a_2 \tau_2^2] + z_- D_- \bar{N}_- [a_1 \tau_1^2 + a_2 \tau_2^2]}{(z_+ D_+ \bar{N}_+ [v_1 a_1 \tau_1 + v_2 a_2 \tau_2] + z_- D_- \bar{N}_- [a_1 \tau_1 + a_2 \tau_2])^2} \\ \text{as } \omega \rightarrow 0. & \end{aligned} \quad [47]$$

In the large ω limit, we have

$$\begin{aligned} \frac{(1-i)L^2}{e^2\beta\sqrt{2\omega}} Z^{-1} \rightarrow & z_+ D_+ \bar{N}_+ [v_1 a_1 \sqrt{\tau_1} + v_2 a_2 \sqrt{\tau_2}] \\ & + z_- D_- \bar{N}_- [a_1 \sqrt{\tau_1} + a_2 \sqrt{\tau_2}] \quad \text{as } \omega \rightarrow \infty, \end{aligned} \quad [48]$$

which fixes one of the two degrees of freedom required to determine an effective FSW element with parameters (Z_∞, τ_∞). We can identify that the correct time constant is $\tau_\infty = \min\{\tau_1, \tau_2\}$ by including the exponentially small terms in the above expansion and in the corresponding FSW limit in 2. In the case that one ion species is negligible in comparison to the other, e.g. $\bar{N}_- \gg \bar{N}_+ > 0$, both τ_0 and τ_∞ can be approximated by the FSW time constant in 36, involving a sensitivity with respect to the non-negligible species. We observed that τ_0 diverged from the single species result for much smaller co-ion particle numbers than τ_∞ (which can remain close to 36 for particle numbers separated by an order of magnitude only).

Time-dependent numerical simulations.—We additionally perform time-dependent simulations of the limit model to validate the semi-analytical impedance expressions. This step validates the numerical scheme itself, which will be used for future investigations of ionic liquids in long nano-pores. The details of the finite-volume scheme, as well as its particular implementation for frequency response simulations, are described in Appendix B. The approach is similar to that utilised by Aslyamov et al.,⁵¹ but we take care to use time-stepping schemes which preserve positivity of particle numbers (a particularly desirable property for simulating pore systems in which some of the ion species can become negligibly small) and use a non-uniform spatial grid to reduce numerical expense.

For our dynamic simulations, we initialise with a system at equilibrium and apply a sinusoidal voltage signal of amplitude $\max_t |\Delta V(t)| = 2.5$ mV. The average surface charge density in the pore is computed by integrating Eq. 21 in x and dividing the result by L (approximated with a rectangle rule for the discretised system). After each period, we estimate the complex impedance by fitting the magnitude, $|Z|$, and phase, $\arg(Z)$, with the input voltage signal and output average surface charge density (fast Fourier transforms can be used when the data is equispaced in time).

Numerical Results

We present results for two parameter sets based on the monovalent ($z_+ = -z_- = 1$) ionic liquids [EMIm][TFSI] and [EMIm][BF₄] at 300 K, summarised in Table I. The relative permittivities (dielectric constants) given in the first row are the static (zero-frequency limit) bulk values obtained by dielectric relaxation spectroscopy,^{64,65} and are assumed fixed for the model ionic liquids. The ion diameters in the second and third rows of Table I are commonly used approximations for the asymmetric molecules under consideration as spherical particles,³¹ while the (constant) self-diffusion coefficients in fourth and fifth rows of Table I are obtained from Vogel–Tammann–Fulcher equations based on data from NMR experiments reported by Noda et al.⁶⁶ The characteristic diffusion timescale is given in the final row of Table I. The parameters for case I were chosen to exemplify an ionic liquid composed of ions with similar sizes (restricted primitive model) with widely differing diffusivities, whereas case II represents ionic liquids exhibiting strong size asymmetry. Bulk densities of the cation and anion are set equal to 2.4 nm^{-3} (3.985 mol L^{-1}), providing the non-dimensional reduced bulk densities $\sigma_+^3 \rho_+^b = \sigma_-^3 \rho_-^b = 0.3$. This is close to the typical value for the ionic liquids which inspired the above parameter sets, and has been considered in other works.³⁸ It follows from the limit model (and the expressions for the complex impedance) that changing the pore length results in a simple rescaling of the impedance response, and so we fix $L = 100 \mu\text{m}$ for our numerical results. All numerical calculations were performed in a non-dimensional framework (see Appendix B). The use of dimensional variables in the figures below allows the comparison of the two ionic liquids (of differing characteristic diffusion times) with ease.

We consider four different DFTs, the simplest of these being the DCA-PB model^{7,67} which is the incorporation of steric hard-wall interactions 14 into the standard PB model (i.e. $F^{\text{HS}} = F^{\text{EC}} = 0$). Without hard-wall effects, contact densities are unrealistically large and the equilibrium problem becomes difficult to resolve numerically, so the standard PB model is not included in our study. We also consider the addition of (White Bear II) hard-sphere terms to the DCA-PB model, which we refer to as the HS-PB model. The two remaining DFTs include all these elements as well as electrostatic correlations, and are identified by the model used for the latter (either BFD or fMSA). Equilibrium density profiles for the four DFTs with ionic liquid I are shown in Fig. 7 in Appendix A.1.

We plot the resistance (real part of the complex impedance) in Fig. 3a and the differential capacitance 31 against frequency in Fig. 3b for ionic liquid II with base voltage $\bar{V} = 0.5$ V. The solid line, computed from the full expression for the complex impedance 44, exhibits a double plateau in Fig. 3a. This is expected for the impedance response of a system with two characteristic times (τ_1, τ_2). The dashed and dotted lines, denoting the results for the low and high frequency effective FSW elements, respectively, bound the solid line above and below. The BFD curves in Fig. 3b show a similar transition from the low to high frequency behavior in the differential capacitance, whereas the asymptotic curves for DCA-PB are very close to the semi-analytical differential capacitance across the full frequency range. The plots for HS-PB and fMSA are similar to those for DCA-PB and BFD shown in the figure, respectively, and so are not included. It is clear from Fig. 3 that the impedance response can deviate significantly from the typical FSW element obtained for a straight slit pore with a simple physical model. The markers in Fig. 3, indicating the results of time-dependent numerical simulations, track the solid line very closely (it is too numerically expensive to simulate the system deeper into the low frequency regime). Beyond the results shown in Fig. 3, we carried out time-dependent numerical simulations for each combination of DFT and ionic liquid, for $W/\sigma_{\pm} = 2, 4, 6, 8$, and a range of frequencies in the interval $0.1 \text{ Hz} < f < 100 \text{ Hz}$. We found a similarly good agreement between the semi-analytical and fully numerical approaches in all cases (data not shown).

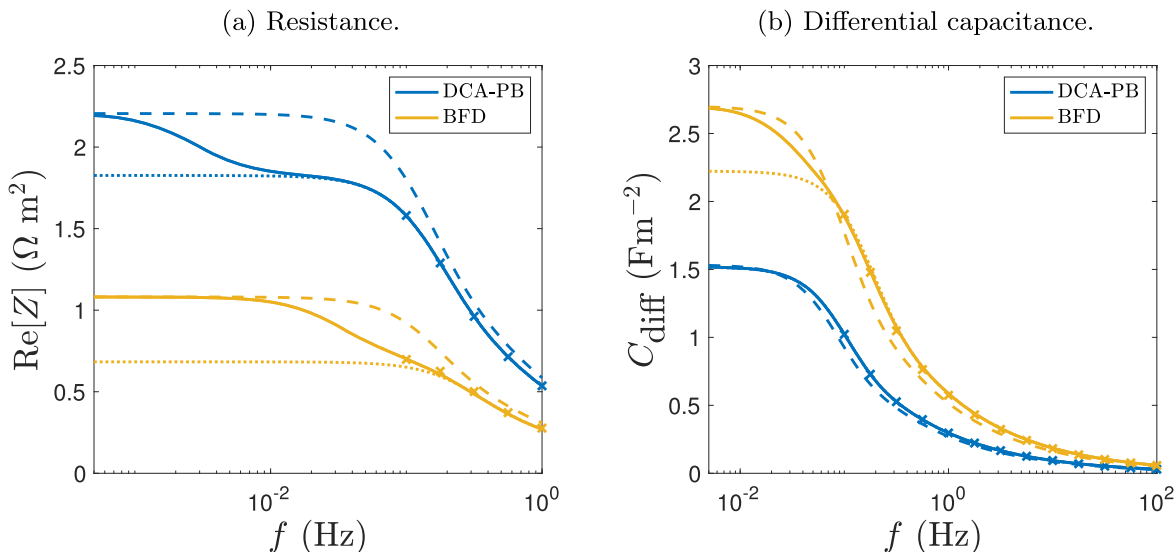


Figure 3. Impedance response for a pore of width $W = 2\sigma_+$ with the parameters of ionic liquid II and $\bar{V} = 0.5$ V. Solid lines correspond to the full semi-analytical result 44, with the dotted and dashed lines indicating the high and low frequency effective FSW elements with parameters (Z_∞, τ_∞) and (Z_0, τ_0) , respectively. The markers denote the results of time-dependent numerical simulations.

In Figs. 4a, 4b, we plot τ_∞ against pore width for each of the four DFTs, again with $\bar{V} = 0.5$ V. The results for the size-symmetric ionic liquid I are shown in Fig. 4a, with the size-asymmetric ionic liquid II in Fig. 4b. The solid and dashed vertical lines in the latter bound the region in which the larger cation cannot enter the slit pore; the value of τ_∞ here is given by Eq. 36. For the BFD and fMSA curves, the transition across the dashed line is smooth since \bar{N}_+ is negligible as $W \rightarrow \sigma_+$ (from above). For the DFTs without electrostatic correlations (DCA-PB and HS-PB), the response time decreases with pore width. When $W > 2\sigma_+$, the values of τ_∞ for these two theories agree quite closely (this is due to the dominance of electrostatic effects for our ionic liquid-inspired parameters, with a larger disparity found for $\epsilon_r = 40$, say). For the DFTs including screening effects, the value of τ_∞ when $W \rightarrow \sigma_-$ is relatively small, with a peak observed at $W = 2\sigma_+$ in Fig. 4a, and a large τ_∞ regime found across $1.25 < W/\sigma_+ < 1.5$ in Fig. 4b. There is good agreement between the results for BFD and fMSA, with a noticeable shift in τ_∞ for the size-asymmetric ionic liquid in Fig. 4b—the shapes of the curves match well, however. We did not expect large differences between the results for the two implementations of electrostatic correlations, as the corresponding equilibrium density profiles are typically very similar (see Fig. 7 in Appendix A.1); the inclusion of correlations by any means has a more significant impact than the particular theory employed. In Figs. 4a and 4b, the high frequency response times for all DFTs converge to similar values for large pore widths ($W \gtrsim 6\sigma_+$).

The corresponding plots for τ_0 are shown in Figs. 4c, 4d. For ionic liquid I in Fig. 4c, we see a significant deviation between the results for DCA-PB and HS-PB across all pore widths, with the latter agreeing closely with BFD and fMSA for $W \gtrsim 4\sigma_+$. For the size-asymmetric case in Fig. 4d, we again see wide peaks in the time constant and a disagreement between the DFTs for large W . While the peaks in τ_∞ appear to be more significant for ionic liquid II, the situation is reversed for τ_0 . Much of the structure of τ_0 for small W is observed in $\partial Q/\partial V$ (as the latter determines one degree of freedom for the low frequency FSW element).

For fMSA we further investigated the dependence of the impedance response on the base voltage \bar{V} , the results of which are presented in Fig. 5. The top/bottom panel corresponds to positive/negative wall potentials, with the results for ionic liquids I and II shown in the left and right panels, respectively. The fMSA lines in Fig. 4 are the curves of smallest magnitude in Figs. 5a, 5b. For the size-symmetric ionic liquid in Figs. 5a, 5c, we see the large

τ_∞ regime widen and shift from $W \approx 2\sigma_+$ for $|\bar{V}| = 0.5$ V toward $W \approx \sigma_+$ as $|\bar{V}|$ is decreased to zero (potential of zero charge). A second peak of smaller magnitude shifts similarly, found at W approximately double that of the first peak, and located at $W \approx 3\sigma_+$ for $\bar{V} = 0$ V. The equilibrium profiles for oppositely signed wall potentials are identical, but with the cation and anion densities swapped. The differences between the corresponding pairs of curves in Figs. 5a, 5c are solely due to the dissimilarity of the single-particle diffusivities for ionic liquid I (found in Table I). For small pores and large potentials, there is a negligible density of co-ions in the pore. In such cases, the ratio of time constants in Figs. 5a, 5c is approximately the ratio of the diffusivities.

The plots for ionic liquid II are shown in Figs. 5b, 5d. Due to the asymmetry of the ion sizes, the equilibrium profiles for oppositely signed \bar{V} cannot be related as for ionic liquid I. Furthermore, the potential of zero charge is a non-zero function of W (bounded between -0.1 V and 0 V for our case). To investigate the influence of the small variation in diffusivities for ionic liquid II, we computed the impedance response for D_+ and D_- set equal to the mean of the diffusivities in Table I. When the density of one species in the pore was negligible, the response times were rescaled according to the change of the single-particle diffusivity of the dominant species. Otherwise, there was an insignificant deviation from the curves shown in Figs. 5b, 5d. We see smooth variation across the dashed vertical line between τ_∞ and the exact single-species result in Fig. 5b, as found for the BFD and fMSA results in Fig. 4b. For negative wall potentials in Fig. 5d, the density of the smaller anions are negligible either side of $W = \sigma_+$, and so the value of τ_∞ is discontinuous as \bar{N}_+ jumps to zero. The values of τ_∞ to the left of the dashed line are not plotted as they correspond to a negligible quantity of ions. As observed for ionic liquid I, there are two large response time regions for the W -interval plotted, which shift as the base voltage varies.

Discussion and Conclusions

We constructed a reduced-order limit model for the dynamics of ionic liquids in long slit pores, incorporating DFT for the equilibrium system and DDFT for the out-of-equilibrium time-evolution. We utilised this model to investigate the dependence of the impedance response on system parameters and the choice of DFT used. A semi-analytical approach was presented for the rapid evaluation of the complex impedance, with the only numerical

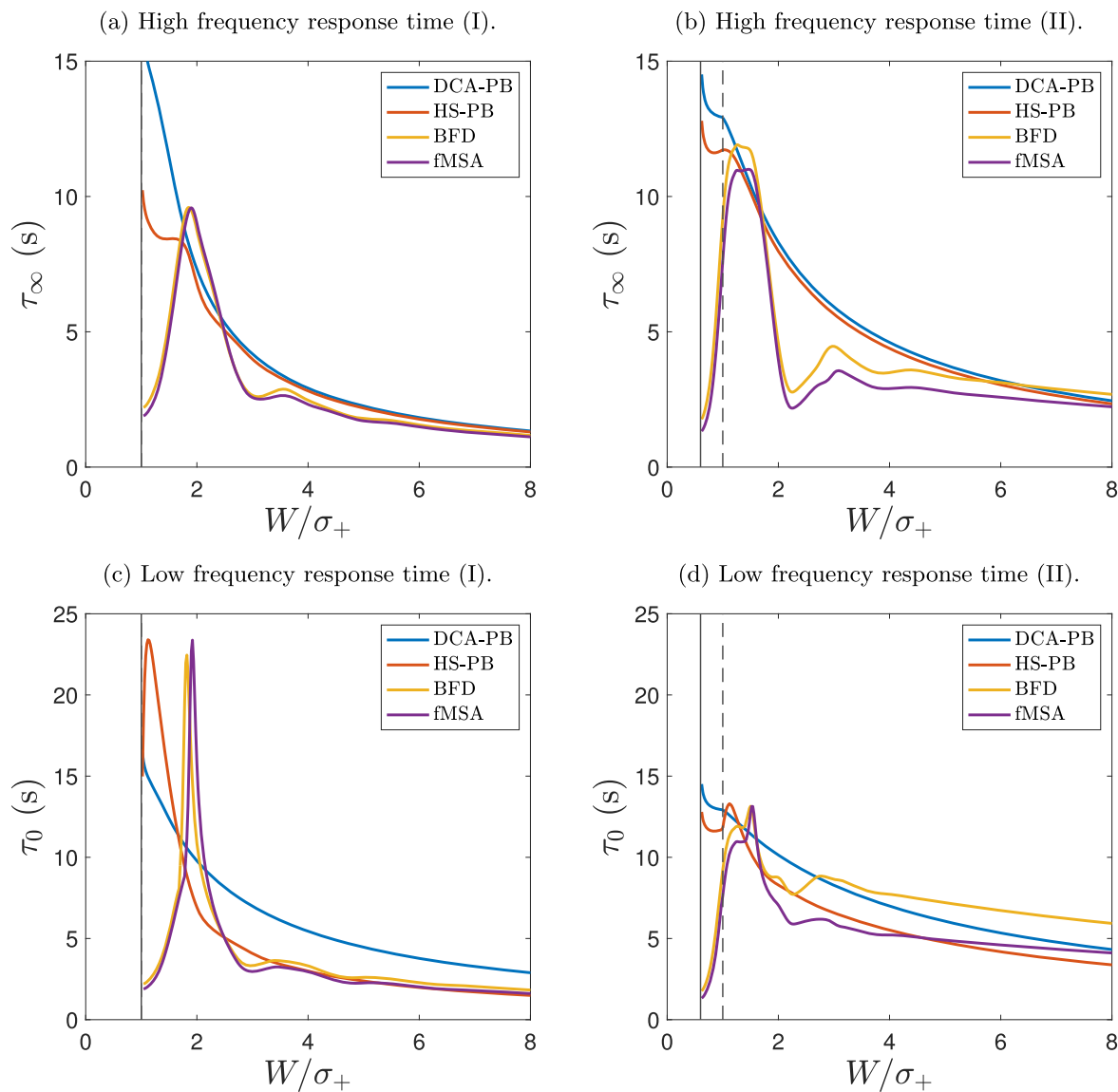


Figure 4. High (a,b) and low (c,d) frequency response time against pore width at $\bar{V} = 0.5$ V. The results for ionic liquid I are shown in panels (a,c), with ionic liquid II in (b,d). The solid curves indicate the effective FSW time constants (τ_∞ and τ_0) for each of the DFTs. The solid vertical lines correspond to the widths below which no ions can fit in the pore, with the dashed vertical lines in panels (b,d) indicating $W = \sigma_+$, below which only the smaller anion can enter the pore. For $\sigma_- < W < \sigma_+$, the curves in panels (b,d) are the exact FSW time constants for the single-ion system 36.

inputs being sensitivities of the equilibrium DFT system. The derived expressions were validated with fully time-dependent numerical simulations.

The impedance response of our reduced-order model can deviate significantly from the FSW element 1, to an extent similar to that found for non-trivial pore geometries with an idealised electrolyte model.⁵⁰ In the high and low frequency limits, we are able to obtain effective FSW elements. We found that the inclusion of electrostatic correlations (which are vital for a physically correct description of the system⁶⁸) drastically modified the predicted high and low frequency response times for pores with widths comparable to one or two ion diameters (see Fig. 4). By varying the base voltage (at which the porescale PEIS was performed), we found that peaks in the FSW time constants shifted toward smaller pore widths as the potential difference magnitude was decreased (see Fig. 5).

As shown in Fig. 6, the charge stored in the pore also varies strongly for small widths as the underlying equilibrium changes. The oscillating dependence on W becomes more dramatic for smaller values of ϵ_r (see the integral capacitance plots of Jiang et al.²⁶ with $\epsilon_r = 1$, for example). For supercapacitor geometries, a good

distribution of pore sizes will provide an optimal balance of total charge storage and charge accessibility for a given application (which determines typical voltage and frequency ranges). For high frequency applications, the total charge stored by the individual electrode pores is relatively less important than their characteristic response times. In addition, the optimisation must respect the total pore fraction available, the fact that thinner pores take up a smaller proportion of the latter, and the shapes of pore size distribution that are feasible to manufacture.

For a positive electrode, Figs. 5a, 5b and 6 describe the dynamic and static charge storage properties of slit pores in the high frequency limit, respectively. For ionic liquid I, we find that peaks τ_∞ and Q coincide for $\bar{V} = 0.5$ V, and so the two optimisation objectives are in conflict (improvements in total capacity result in reduced accessibility). Slit pores with $W \approx \sigma_+$ have lower response times without a significant reduction in charge stored. For ionic liquid II, the optimisation objectives appear to be non-conflicting. Pores of width close to σ_- provide large values of Q as well as fast response times, and for $W \approx 1.5\sigma_+$, both the static and dynamic charge storage properties are relatively poor. It is clear that the

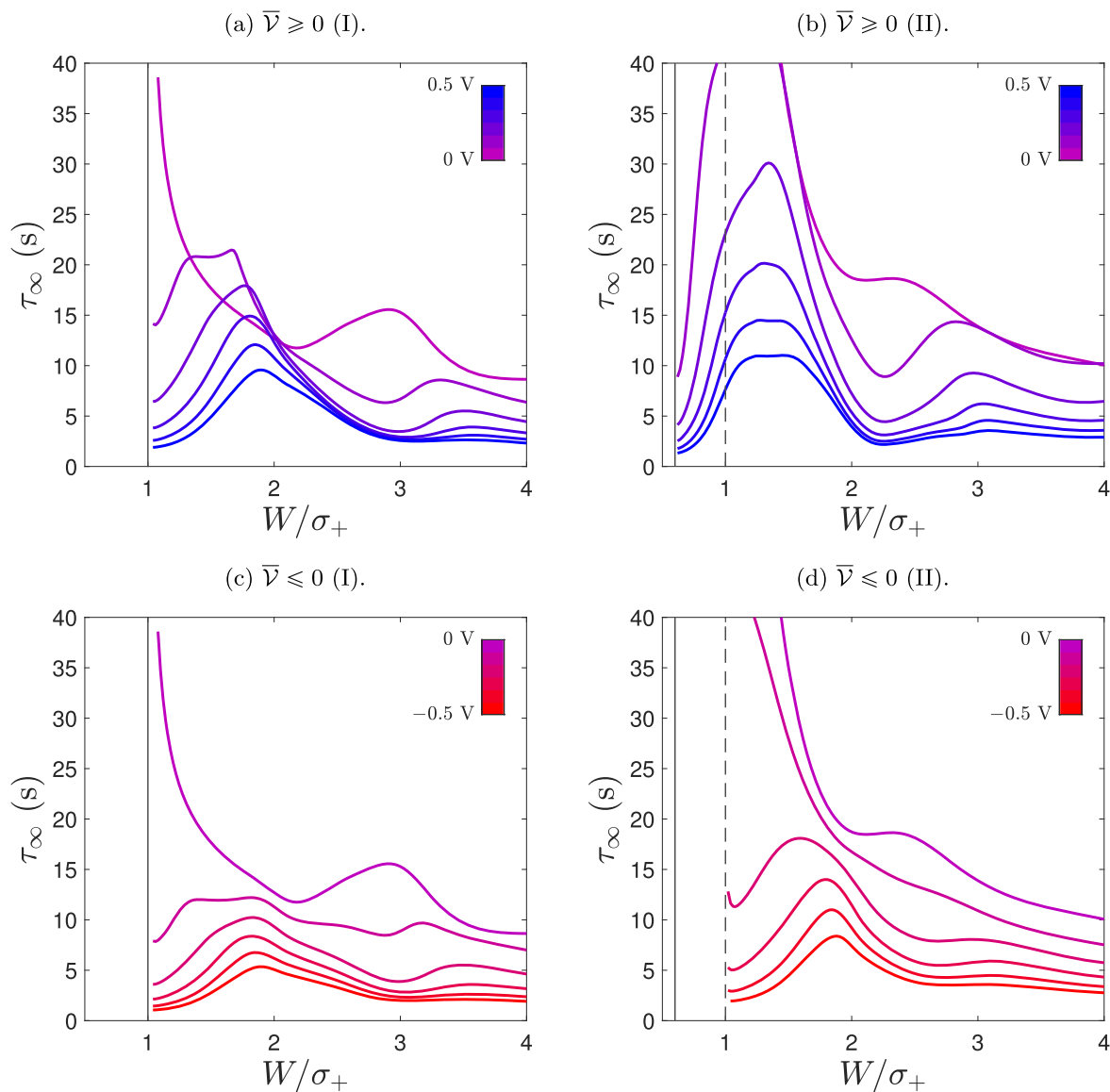


Figure 5. High frequency response time against pore width for a range of \bar{V} with FMSA for the DFT. Panels (a,b) show curves corresponding to $\bar{V} = 0, 0.1, 0.2, 0.3, 0.4, 0.5$ V, with $-\bar{V} = 0, 0.1, 0.2, 0.3, 0.4, 0.5$ V in panels (c,d). The left/right panels correspond to ionic liquid I/II, with the solid and dashed vertical lines as in Fig. 4.

presented theory (along with consideration of nonlinear responses⁵¹) adds to the pool of information on which the optimisation of supercapacitor geometries can be based.

The model for the ionic liquid can be generalised with ease to incorporate non-constant permittivities and diffusivities; molecular dynamics and mean-field simulations have shown that confinement can cause significant variations in these quantities.^{69,70} Relevant DDFT studies include the incorporation of density-dependent permittivities,⁷¹ and the theoretical investigation of packing fraction-dependent diffusivities.⁷² Inclusion of tortuosity effects is also kept for future work. Overall, the approach presented here is clearly applicable to more general particle systems or other models of ionic liquids; the asymptotic reduction of the DDFT system is an application of lubrication theory, and can be carried out for a large class of dynamical equations in long slit pores. The resulting limit model may then also be amenable to a semi-analytical impedance calculation. Moreover, the sensitivities appearing in the analysis we present can even be computed from molecular simulations.

We believe that modifications to the DDFT will be required to accurately model ion dynamics in long cylindrical pores. For the simple case of a single species hard-sphere fluid in single-file transport, particles

can pass through each other when the time evolution is governed by the DDFT Eq. 4.³⁴ In a slit pore, on the other hand, it can be thought that the ions slide past each other in the unbounded direction perpendicular to the x - y plane. Extensions of Eq. 4 may be required to simulate pore systems further from equilibrium (e.g. nonlinear electrochemical impedance spectroscopy). One option is provided by the recently developed power functional theory³⁵ which generalises standard DDFT by including non-adiabatic effects ignored by the DDFT assumption 6.

Lastly, we note that the limit model presented can be used as the basis for a simplified cell-level model, in which a set of pores representing each electrode are directly coupled to the separator region (with a modification of the entrance boundary condition 22), akin to the simplified model presented by Kondrat and Kornyshev⁹ which ignores the pore-size hierarchy typical of electrode geometries; this parallels the many-particle models studied by Kirk et al.⁷³ for Li-ion batteries. The time-dependent simulation approach detailed in Appendix B was only used for validation in the present work, but for geometries more complex than a single straight pore, for which the system is likely analytically intractable, time-dependent simulations may be the only viable approach. It would be of interest to improve the resolution of the system at pore entrances and

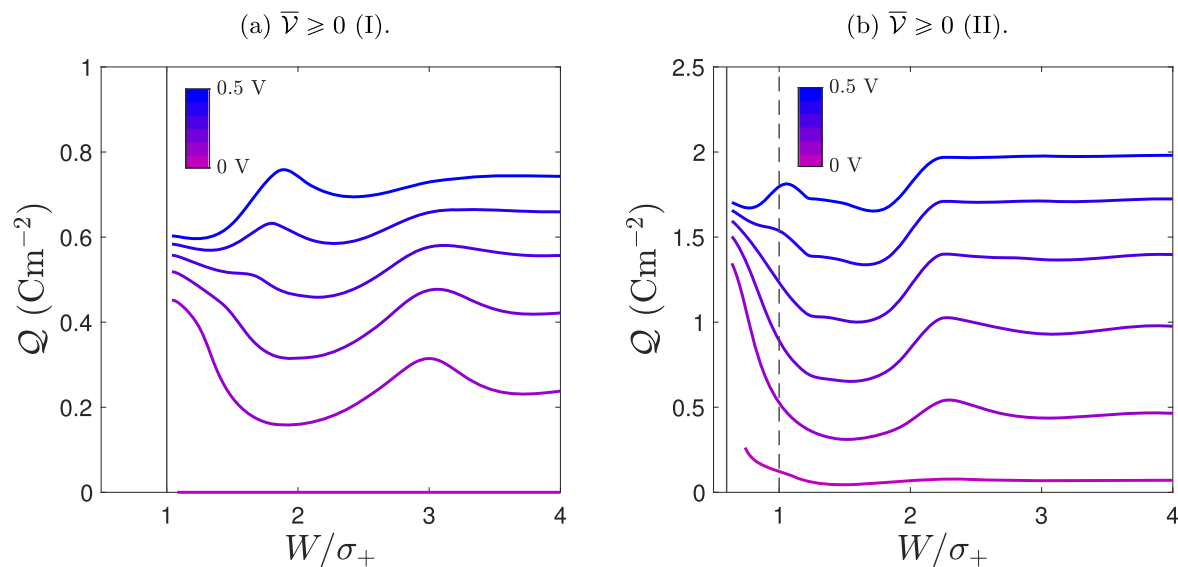


Figure 6. Charge stored at equilibrium (per unit of pore length and depth) against pore width for a range of $\bar{\mathcal{V}} \geq 0$ with fMSA for the DFT. The curves are analogous to those of τ_{∞} in Figs. 5a, 5b—see the caption for details. Note the difference in vertical axes between the two panels.

branchings which could involve a hybridisation of the limit model with a 2D DDFT solver; we have also considered hybridisation with molecular simulations as done for compressible nanoscale flows.⁷⁴

Acknowledgments

RJT, TR and MM acknowledge support from the Innovate UK WIZER project (TS/S005811/1). TR greatly acknowledges the financial support provided by the Science and Engineering Research Board (SERB), Government of India (SRG/2021/000741). TLK was supported by the EPSRC Faraday Institution Multiscale Modelling project (EP/S003053/1, grant number FIRG025). RJT is grateful to Dr. Mohammad Kamalvand for providing validation data.

Appendix A. Numerical Details

We first discuss the solver for the 1D DFTs required to compute equilibrium solutions and their numerical sensitivities for the semi-analytical impedance expressions, and employed as a component of the numerical scheme for time-dependent simulations. We then outline the finite-volume approach for the latter, its implementation for impedance response experiments, and provide the results of validation tests.

A.1. Equilibrium Solver.—In the present work, we perform both canonical and grand canonical equilibrium calculations (predominantly the former). In the canonical case, we are given particle numbers N_i and a wall surface potential \mathcal{V} , from which we compute 1D equilibrium densities $\rho_i(y)$ and constant chemical potentials μ_i . In the grand canonical case, the μ_i are inputs and the N_i can be trivially computed by integrating the output densities. Both situations are tackled with a Picard iteration (iterative substitution) scheme with a line search based on the fixed-point problem 9 as described by Knepley et al.⁷⁵ and Roth,⁵⁸ which does not require the evaluation of Eq. 5 to obtain Ω at any stage. During each Picard iteration, we solve the PB equation for the electrostatic potential $\psi(y)$ arising from the substitution of Eqs. 9, 11 into the Poisson equation 12. This is significantly more robust than solving the Poisson equation with iteration-lagged densities on the right hand side. For canonical computations, we augment the PB iteration scheme with the integral expression for the particle numbers 18, solving for the unknown μ_i in conjunction with the electrostatic potential. Specifically, if $\rho_i^{(k)}$ denotes the k th Picard iteration of the density for species i , we first build

$$g_i^{(k)} = \exp \left[-\beta \left(\left. \frac{\delta F^{\text{HS}}}{\delta \rho_i} \right|_{\rho_i^{(k)}} + \left. \frac{\delta F^{\text{EC}}}{\delta \rho_i} \right|_{\rho_i^{(k)}} + U_i^{\text{HW}} \right) \right]. \quad [\text{A}\cdot 1]$$

Given N_i , we solve an augmented PB system for $\rho_i^{(k+1)}(y)$ and $\mu_i^{(k+1)}$,

$$\begin{aligned} \rho_i^{(k+1)} &= g_i^{(k)} \exp[-\beta(ez_i\psi^{(k+1)} - \mu_i^{(k+1)})], \\ \epsilon_0 \epsilon_r \psi_{yy}^{(k+1)} &= -e \sum_i z_i \rho_i^{(k+1)}, \end{aligned}$$

$$N_i = \int_0^W \rho_i^{(k+1)} dy, \quad [\text{A}\cdot 2]$$

with the boundary conditions for the electrostatic potential 13. The above system can be solved with fast gradient descent algorithms as in the unaugmented case. We found this approach to be more robust than including the particle number constraint 18 into the Euler–Lagrange equation 6 using a Lagrange multiplier.^{76,77} For the BFD and fMSA theories, which take a set of constant charge-neutral ion densities as inputs, we use the bulk densities external to the pore, ρ_i^b , even when the system is not in equilibrium.

The electrostatic component of the external potential, U_i^{ES} (omitted above for brevity), is a function of the surface charge density, not the surface potential;⁷⁸ according to the uniqueness theorem of Evans,¹⁰ fixing (Q_0, Q_W) uniquely determines the equilibrium densities in a planar geometry. However, the same cannot be said when prescribing surface potentials as in the present work, and the surface charge–potential relation is known to be non-monotonic for certain parameters (which would provide more than one distinct equilibrium for some values of the wall potential). For this reason, it is not ensured that $Q_0 = Q_W$, or equivalently that the density profiles are symmetric about the pore centreline, $y = W/2$. Accordingly, all equilibrium profiles are solved for in a full pore, rather than a half pore with $\psi_{y|y=W/2} = 0$ (as is common in the literature), however, we did not observe any symmetry breaking or multiplicity of equilibria for the parameters considered here.

The equilibrium solver was carefully checked against results from a number of different sources (e.g. independently written DFT code for identical systems), and thus is not the subject of the numerical validations below. Throughout, the equilibria are

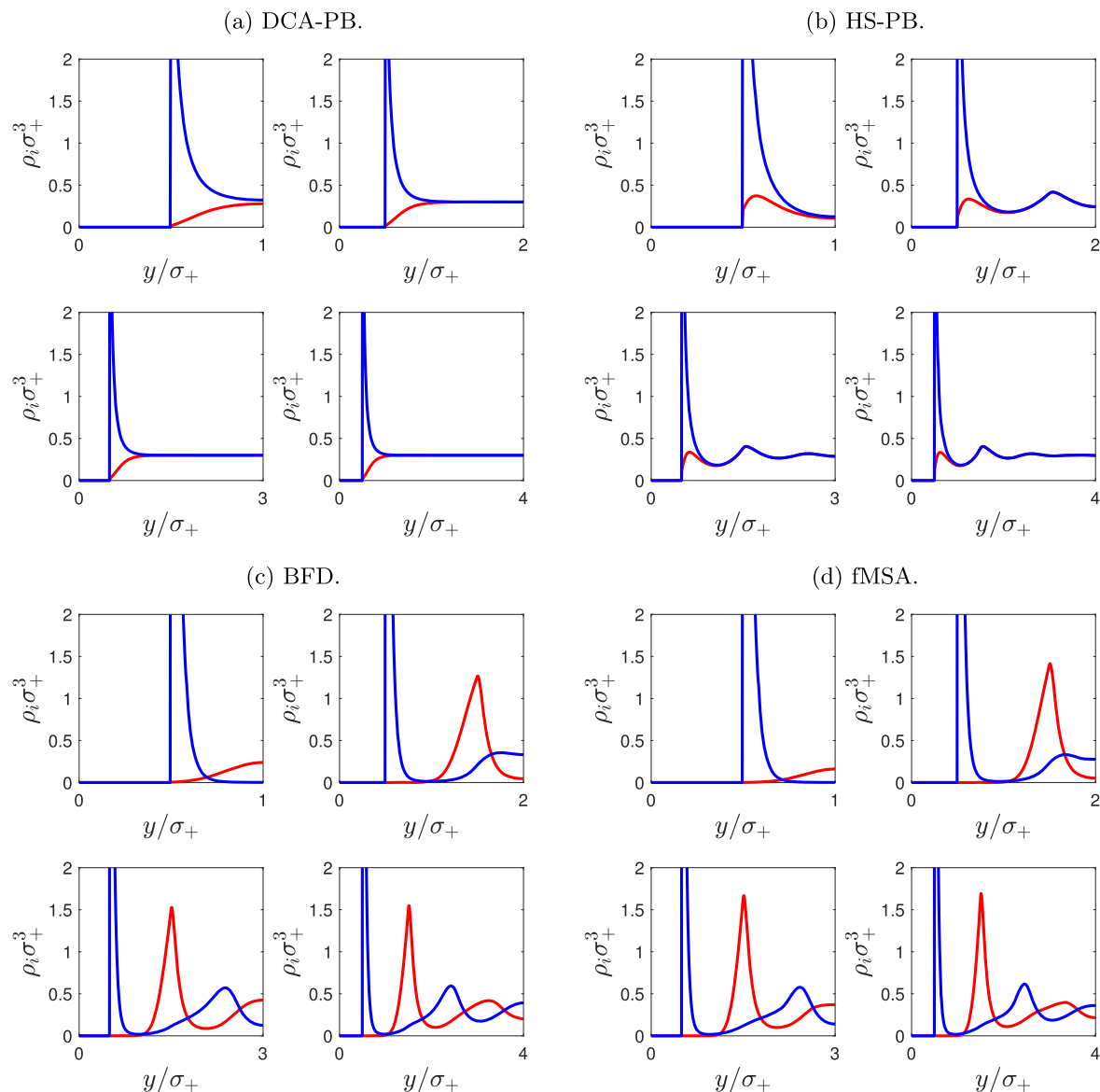


Figure 7. Equilibrium densities for the four DFTs with parameters for ionic liquid I. Each panel displays four sets of ion profiles (symmetric about the pore centerline) with $W/\sigma_+ = 2, 4, 6, 8$ (corresponding to 1, 2, 3, 4 nm, respectively). The potential on the pore walls is fixed at 0.5 V. The cation/anion densities are plotted in red/blue.

computed using a discretisation in y of 400 grid points per nanometer, giving 200 and 120 grid points across the diameters of the $[\text{EMIm}]^+ / [\text{TFSI}]^-$ and $[\text{BF}_4]^-$ ions, respectively. The tolerances of the PB solver and Picard iteration were chosen to be sufficiently small that they are not limiting the accuracy of the equilibrium solution. The surface charge density on the pore walls differed by at most 2% from the fully converged result.

Equilibrium density profiles for ionic liquid I (see Table I) are presented in Fig. 7 for the four DFTs considered in this work. The left half pore is plotted as the profiles are symmetric about the pore centreline. For these grand canonical calculations, we have fixed the chemical potential equal to the bulk value (determined by $\rho_i^b \sigma_+^3 = 0.3$), and set the pore surface potential to 0.5 V. The ion layering induced by the addition of hard-sphere terms is clear from a comparison of Fig. 7a and Fig. 7b, while the addition of electrostatic correlations introduced in Figs. 7c, 7d disrupts the local charge neutrality seen in Figs. 7a, 7b. There is good agreement between the two implementations of electrostatic correlations, with a slight difference in amplitude of the density profiles shown in Figs. 7c, 7d.

Appendix B. Time-Dependent Simulations of the Limit Model

For the following, we move to a non-dimensional system by rescaling with

$$(x, y) = \sigma_+(x^*, y^*), \quad \rho_i = \sigma_+^{-3} \rho_i^*, \quad t = \frac{\sigma_+^2}{D_+} t^*, \quad \mu_i = \beta^{-1} \mu_i^*, \quad [\text{B.3}]$$

and dropping the stars. Here, and for our other numerical calculations, we have used the cation diameter σ_+ , the cation diffusion time σ_+^2/D_+ , and the inverse thermodynamic temperature β^{-1} as our reference length, time, and energy scales, respectively. This particular rescaling is chosen as it is fixed for a given ionic liquid and temperature (independent of input frequency). The limit model 19 becomes

$$\frac{\partial N_i}{\partial t} = \mathcal{D}_i \frac{\partial}{\partial x} \left(N_i \frac{\partial \mu_i}{\partial x} \right), \quad [\text{B.4}]$$

where $\mathcal{D}_i = D_i/D_+$ are non-dimensional diffusion coefficients.

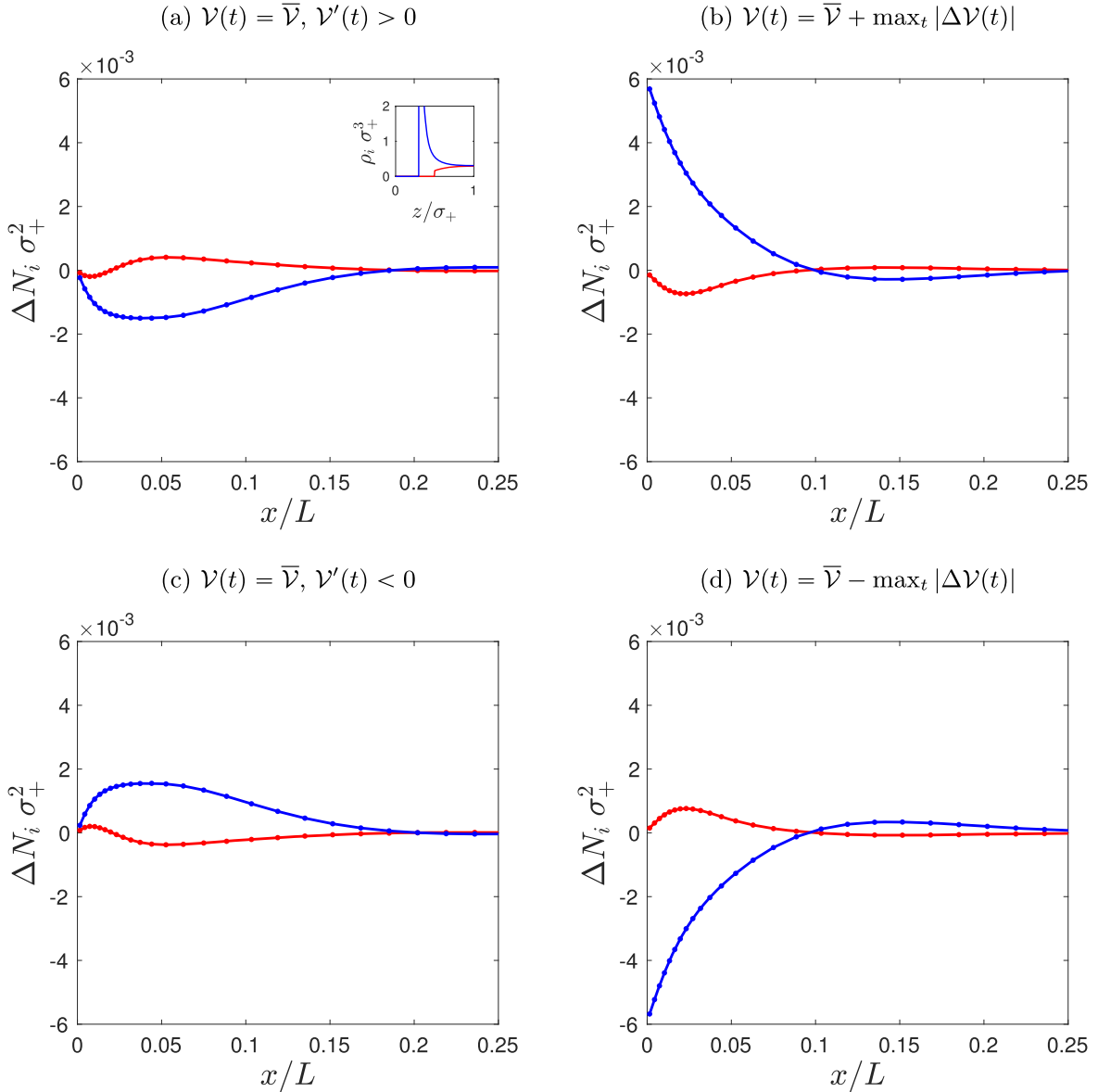


Figure 8. Perturbation particle numbers at different stages of a frequency response simulation with $f = 10$ Hz. The slit pore considered has width $W = 1$ nm and length $L = 100 \mu\text{m}$, and the applied wall potential is defined by $\bar{\mathcal{V}} = 0.5$ V, $\max_t |\Delta\mathcal{V}(t)| = 2.5$ mV. We use the parameters for ionic liquid II from Table I and the DCA-PB model, with the unperturbed equilibrium profile inset in panel (a). The cation/anion particle numbers are plotted in red/blue.

We discretise the slit pore in the length variable x by sub-dividing into cells (finite volumes), where the end points of cell j are denoted $x_{j-1/2}$ and $x_{j+1/2}$, with midpoint x_j . Starting with particle numbers in each cell at time t , $N_i^j(t)$, the 1D densities $\rho_i^j(y, t)$ and chemical potentials $\mu_i^j(t)$ are calculated as outlined above. The computational complexity of this step is mitigated significantly by parallelisation, and the fact that the equilibrations are initialised with the densities from the previous time-step (the profiles ρ_i^j serve no further purpose in the following).

To evolve the particle numbers in time according to Eq. B-4, we employ the mass-conserving finite-volume scheme outlined by Carrillo et al.⁷⁹ which has recently been employed for the numerical simulation of a DDFT system.⁸⁰ Multiplying Eq. B-4 by an indicator function for cell j (defined by $\zeta^j(x) = 1$ for $x \in [x_{j-1/2}, x_{j+1/2}]$ and zero otherwise) and integrating yields an exact analytical expression for the rate of change of the total particle number of each ion species in cell j in terms of continuous fluxes,

$$\frac{d}{dt} \int_{x_{j-1/2}}^{x_{j+1/2}} N_i dx = \mathcal{D}_i \left[N_i \frac{\partial \mu_i}{\partial x} \right]_{x_{j-1/2}}^{x_{j+1/2}}. \quad [\text{B.5}]$$

Substituting $N_i = N_i^j(t)$ in the left hand side of B-5 and defining $\Delta x_j = x_{j+1/2} - x_{j-1/2}$, we approximate this exact integral balance with

$$\frac{d}{dt} N_i^j = \frac{f_i^{j+1/2} - f_i^{j-1/2}}{\Delta x_j}, \quad [\text{B.6}]$$

where we have defined the numerical inter-cell fluxes

$$f_i^{j\pm 1/2} \approx \mathcal{D}_i \left(N_i \frac{\partial \mu_i}{\partial x} \right) \Big|_{x_{j\pm 1/2}}. \quad [\text{B.7}]$$

To calculate the numerical fluxes, we utilise positivity preserving piecewise linear reconstructions of the particle numbers. Fixing time

Table II. Numerical convergence of the complex impedance ($\Omega \text{ m}^2$) for the same parameters as in Fig. 8—see the caption for details. Dashes denote non-convergence. The semi-analytical result is approximately $0.1695 - 0.1695i$.

		# of time-steps per period		
		250	1000	4000
# of cells	8	0.1996 – 0.1705i	0.1988 – 0.1716i	0.1985 – 0.1719i
	16	0.1775 – 0.1723i	0.1766 – 0.1731i	0.1764 – 0.1733i
	32	—	0.1710 – 0.1702i	0.1708 – 0.1704i
	64	—	—	0.1695 – 0.1697i

t (and dropping its dependence from our notation), we define

$$\tilde{N}_i^j(x) = N_i^j + (x - x_j)\eta_i^j, \quad [\text{B.8}]$$

where η_i^j is the slope of the reconstruction. We employ the minmod limiter,

$$\eta_i^j = \text{minmod}\left(\frac{N_i^{j+1} - N_i^j}{x_{j+1} - x_j}, \frac{N_i^j - N_i^{j-1}}{x_j - x_{j-1}}\right), \quad [\text{B.9}]$$

where the minmod operator is defined by⁷⁹

$$\text{minmod}(y_1, y_2, \dots) := \begin{cases} \min\{y_1, y_2, \dots\} & \text{if } y_k > 0 \forall k, \\ \max\{y_1, y_2, \dots\} & \text{if } y_k < 0 \forall k, \\ 0 & \text{otherwise.} \end{cases} \quad [\text{B.10}]$$

In simple terms, the slope B.9 is set equal to zero at a turning point or otherwise chosen to be the one-sided finite difference with the smallest absolute value (minimum modulus). It follows that the reconstructed $\tilde{N}_i^j(x)$ are non-negative within cell j . A generalised minmod limiter involving both one-sided and central finite differences with a tuneable numerical viscosity has been used by other authors.^{79,80} Using such reconstructions, we can approximate N_i at the cell boundaries $x_{j\pm 1/2}$ required to compute the fluxes B.7. Following the notations of Carrillo et al.,⁷⁹ we define the reconstructed particle numbers at the East and West boundaries of a cell,

$$\begin{aligned} N_i^{j,W} &= \tilde{N}_i^j(x_{j-1/2}) = N_i^j - \frac{\Delta x_j}{2}\eta_i^j, \\ N_i^{j,E} &= \tilde{N}_i^j(x_{j+1/2}) = N_i^j + \frac{\Delta x_j}{2}\eta_i^j. \end{aligned} \quad [\text{B.11}]$$

For the chemical potential component of the fluxes B.7 we take a simple finite difference, and define the numerical velocities

$$-u_i^{j-1/2} = \mathcal{D}_i\left(\frac{\mu_i^j - \mu_i^{j-1}}{x_j - x_{j-1}}\right). \quad [\text{B.12}]$$

We use an upwind scheme in space, choosing the flux

$$-f_i^{j-1/2} = u_i^{j-1/2} \begin{cases} N_i^{j-1,E} & \text{if } u_i^{j-1/2} \geq 0, \\ N_i^{j,W} & \text{if } u_i^{j-1/2} < 0, \end{cases} \quad [\text{B.13}]$$

which can be written equivalently as

$$-f_i^{j-1/2} = \max\{u_i^{j-1/2}, 0\}N_i^{j-1,E} + \min\{u_i^{j-1/2}, 0\}N_i^{j,W}. \quad [\text{B.14}]$$

The positivity of the particle numbers can be ensured if strongly stability preserving (SSP) schemes are used for the time discretisation, subject to the appropriate Courant–Friedrichs–Lewy (CFL) condition. We use the forward Euler scheme with the CFL condition

$$\Delta t \cdot \max_j \left\{ \frac{u_i^{j+1/2}}{\Delta x_j}, -\frac{u_i^{j-1/2}}{\Delta x_j} \right\} \leq \frac{1}{2}. \quad [\text{B.15}]$$

This result is valid for any choice of positivity preserving piecewise linear reconstruction, and the proof relies on the useful property that $N_i^j = (N_i^{j,E} + N_i^{j,W})/2$. The time-step is chosen adaptively to satisfy the dynamic constraint B.15, however this CFL condition is not sufficient to ensure stability of the numerical scheme. We performed validation tests with higher-order multi-step SSP Runge–Kutta schemes, which are too computationally expensive to be used instead of the Euler scheme due to the increased number of DFT solves without a significant easing of time-step requirements.

B.1. Implementation for frequency response simulations.—

Our implementation of the above numerical scheme is tuned for frequency response simulations; a different set-up may be more appropriate for other experiment types. For a given frequency, the perturbation to the particle numbers reaches a distance into the pore characterised by the penetration depth $\ell = \sqrt{\max\{D_i\}/\omega}$. At sufficiently low frequencies for which $\ell \approx L$, the no-flux boundary at the pore cap begins to influence the dynamics and the resulting impedance behavior.^{49,50} In order to attain a numerically efficient discretisation of the pore, the cell widths, Δx_j , should be chosen according to ℓ . For this, we use a convex stretching function which maps a set of equidistant points in the interval $[0, 1]$ to a distribution of cell midpoints in $[0, L]$, providing three levels of spatial resolution in the pore length; the highest resolution is attained in a layer of width 4ℓ adjacent to the pore entrance, good resolution in the region $[4\ell, 75\ell]$, and sparsely distributed cell midpoints beyond this (as the densities remain relatively close to equilibrium in this region). As ℓ increases, the three grades of resolution transition to two, and eventually the spatial discretisation becomes uniform. In order to obtain convergent numerical simulations, we need a more strict time-step constraint than the CFL condition B.15. For a fixed spatial discretisation, the time-step required for numerical stability depends on the frequency imposed. At high frequencies, the number of time-steps per period must be sufficiently large, whereas for low frequencies, a frequency-independent time-step is needed; explicitly, in addition to B.15, we use a constraint of the form

$$\Delta t \leq \min\{\Delta t_1, 1/\nu\}, \quad [\text{B.16}]$$

where Δt_1 denotes the frequency-independent upper bound on the time-step and ν is the desired minimum number of time-steps per period.


In Fig. 8 we present snapshots of the particle number perturbations in a slit pore undergoing a frequency response simulation. The four panels correspond to the two zeros and two peaks of the voltage perturbation in a single period. The density profiles inset in Fig. 8a show that the pore holds more anions than cations, with $\bar{N}_+ \sigma_+^2 = 0.260$ and $\bar{N}_- \sigma_-^2 = 1.34$, and all panels of Fig. 8 show that the anion deviation $\Delta N_+ \sigma_+^2$ (plotted in blue) is generally of larger amplitude than the cation deviation. The different levels of

numerical resolution can be seen from the clustering of the cell midpoints, indicated by the points on the curves.


B.2. Numerical validation.—In Table II, we provide the calculated complex impedance for the same case as in Fig. 8 with different spatial and temporal discretisations. The time-step is proportional to the reciprocal of the number of time-steps per period (columns), and the non-uniform spatial increments are proportional to the reciprocal of the number of cells (rows). As expected for a system with similarities to the standard diffusion equation, increasing the spatial resolution by a factor of n (down the rows of Table II) requires a decrease in the time-step by a factor of n^2 (across the columns) for the scheme to converge numerically. As long as the time-step is sufficiently small for numerical stability, decreasing it further does not result in a significant change to the computed complex impedance. With 32 cells and 1000 time-steps per period, the complex impedance deviates by less than 1% from the semi-analytical result, $Z \approx 0.1695 - 0.1695i$. For the results of the time-dependent simulations presented in the main text, we typically discretised the pore with 32 or 64 cells, depending on the numerical complexity of the DFT to be solved in each cell. For very low frequencies only 16 finite volumes are used as the particle numbers along the pore are close to uniform and otherwise the simulation times become excessively long.

ORCID

Ruben J. Tomlin  <https://orcid.org/0000-0002-4852-9953>

Tribeni Roy  <https://orcid.org/0000-0002-6093-8346>

Toby L. Kirk  <https://orcid.org/0000-0002-6700-0852>

Monica Marinescu  <https://orcid.org/0000-0003-1641-3371>

Dirk Gillespie  <https://orcid.org/0000-0003-0802-5352>

References

- M. W. Verbrugge and P. Liu, "Microstructural analysis and mathematical modeling of electric double-layer supercapacitors." *J. Electrochem. Soc.*, **152**, D79 (2005).
- M. Kroupa, G. J. Offer, and J. Kosek, "Modelling of supercapacitors: factors influencing performance." *J. Electrochem. Soc.*, **163**, A2475 (2016).
- I. Borukhov, D. Andelman, and H. Orland, "Steric effects in electrolytes: a modified Poisson-Boltzmann equation." *Phys. Rev. Lett.*, **79**, 435 (1997).
- M. S. Kilic, M. Z. Bazant, and A. Ajdari, "Steric effects in the dynamics of electrolytes at large applied voltages. I. Double-layer charging." *Physical Review E*, **75**, 021502 (2007).
- A. A. Kornyshev, "Double-layer in ionic liquids: a paradigm change?" *The Journal of Physical Chemistry B*, **111**, 5545 (2007).
- M. S. Kilic, M. Z. Bazant, and A. Ajdari, "Steric effects in the dynamics of electrolytes at large applied voltages. II. Modified Poisson-Nernst-Planck equations." *Physical Review E*, **75**, 021503 (2007).
- D. Gillespie, "A review of steric interactions of ions: why some theories succeed and others fail to account for ion size." *Microfluidics and Nanofluidics*, **18**, 717 (2015).
- M. Z. Bazant, B. D. Storey, and A. A. Kornyshev, "Double layer in ionic liquids: overscreening vs crowding." *Phys. Rev. Lett.*, **106**, 046102 (2011).
- S. Kondrat and A. Kornyshev, "Charging dynamics and optimization of nanoporous supercapacitors." *The Journal of Physical Chemistry C*, **117**, 12399 (2013).
- R. Evans, "The nature of the liquid-vapour interface and other topics in the statistical mechanics of non-uniform, classical fluids." *Adv. Phys.*, **28**, 143 (1979).
- R. Evans, "Density functionals in the theory of nonuniform fluids." *Fundamentals of Inhomogeneous Fluids*, **1**, 85 (1992).
- J. F. Lutsko, "Recent developments in classical density functional theory." *Adv. Chem. Phys.*, **144**, 1 (2010).
- Y. Rosenfeld, "Free-energy model for the inhomogeneous hard-sphere fluid mixture and density-functional theory of freezing." *Phys. Rev. Lett.*, **63**, 980 (1989).
- Y.-X. Yu and J. Wu, "Structures of hard-sphere fluids from a modified fundamental-measure theory." *J. Chem. Phys.*, **117**, 10156 (2002).
- R. Roth, R. Evans, A. Lang, and G. Kahl, "Fundamental measure theory for hard-sphere mixtures revisited: the White Bear version." *J. Phys.: Condens. Matter*, **14**, 12063 (2002).
- H. Hansen-Goos and R. Roth, "Density functional theory for hard-sphere mixtures: the White Bear version mark II." *J. Phys.: Condens. Matter*, **18**, 8413 (2006).
- L. Blum, "Mean spherical model for asymmetric electrolytes: I. Method of solution." *Mol. Phys.*, **30**, 1529 (1975).
- L. Mier-y Teran, S. H. Suh, H. S. White, and H. T. Davis, "A nonlocal free-energy density-functional approximation for the electrical double layer." *J. Chem. Phys.*, **92**, 5087 (1990).
- Z. Tang, L. Mier-y Teran, H. T. Davis, L. E. Scriven, and H. S. White, "Non-local free-energy density-functional theory applied to the electrical double layer: part I: symmetrical electrolytes." *Mol. Phys.*, **71**, 369 (1990).
- L. Mier-y Teran, Z. Tang, H. T. Davis, L. E. Scriven, and H. S. White, "Non-local free-energy density-functional theory applied to the electrical double layer: part II: 2: 1 electrolytes." *Mol. Phys.*, **72**, 817 (1991).
- E. Kierlik and M. L. Rosinberg, "Density-functional theory for inhomogeneous fluids: adsorption of binary mixtures." *Phys. Rev. A*, **44**, 5025 (1991).
- Y. Rosenfeld, "Free energy model for inhomogeneous fluid mixtures: Yukawa-charged hard spheres, general interactions, and plasmas." *J. Chem. Phys.*, **98**, 8126 (1993).
- D. Gillespie, W. Nonner, and R. S. Eisenberg, "Coupling Poisson-Nernst-Planck and density functional theory to calculate ion flux." *J. Phys.: Condens. Matter*, **14**, 12129 (2002).
- D. Gillespie, W. Nonner, and R. S. Eisenberg, "Density functional theory of charged, hard-sphere fluids." *Physical Review E*, **68**, 031503 (2003).
- R. Roth and D. Gillespie, "Shells of charge: a density functional theory for charged hard spheres." *J. Phys.: Condens. Matter*, **28**, 244006 (2016).
- D.-E. Jiang, Z. Jin, and J. Wu, "Oscillation of capacitance inside nanopores." *Nano Lett.*, **11**, 5373 (2011).
- D.-E. Jiang, D. Meng, and J. Wu, "Density functional theory for differential capacitance of planar electric double layers in ionic liquids." *Chem. Phys. Lett.*, **504**, 153 (2011b).
- D.-E. Jiang, Z. Jin, D. Henderson, and J. Wu, "Solvent effect on the pore-size dependence of an organic electrolyte supercapacitor." *J. Phys. Chem. Letters*, **3**, 1727 (2012).
- K. Liu, C. Lian, D. Henderson, and J. Wu, "Impurity effects on ionic-liquid-based supercapacitors." *Mol. Phys.*, **115**, 454 (2017).
- C. Lian, K. Liu, K. L. Van Aken, Y. Gogotsi, D. J. Wesolowski, H. L. Liu, D. E. Jiang, and J. Z. Wu, "Enhancing the capacitive performance of electric double-layer capacitors with ionic liquid mixtures." *ACS Energy Lett.*, **1**, 21 (2016).
- J. N. Neal, D. J. Wesolowski, D. Henderson, and J. Wu, "Ion distribution and selectivity of ionic liquids in microporous electrodes." *J. Chem. Phys.*, **146**, 174701 (2017).
- W. Dieterich, H. L. Frisch, and A. Majhofer, "Nonlinear diffusion and density functional theory." *Zeitschrift für Physik B Condensed Matter*, **78**, 317 (1990).
- U. M. B. Marconi and P. Tarazona, "Dynamic density functional theory of fluids." *J. Chem. Phys.*, **110**, 8032 (1999).
- M. te Vrugt, H. Löwen, and R. Wittkowski, "Classical dynamical density functional theory: from fundamentals to applications." *Adv. Phys.*, **69**, 121 (2020).
- M. Schmidt and J. M. Brader, "Power functional theory for Brownian dynamics." *J. Chem. Phys.*, **138**, 214101 (2013).
- J. Jiang, D. Cao, D.-E. Jiang, and J. Wu, "Time-dependent density functional theory for ion diffusion in electrochemical systems." *J. Phys.: Condens. Matter*, **26**, 284102 (2014).
- C. Lian, S. Zhao, H. Liu, and J. Wu, "Time-dependent density functional theory for the charging kinetics of electric double layer containing room-temperature ionic liquids." *J. chem. phys.*, **145**, 204707 (2016).
- L. Qing, S. Zhao, and Z.-G. Wang, "Surface charge density in electrical double layer capacitors with nanoscale cathode-anode separation." *J. Phys. Chem. B*, **125**, 625 (2021).
- S. Babel, M. Eikerling, and H. Löwen, "Impedance resonance in narrow confinement." *J. Phys. Chem. C*, **122**, 21724 (2018).
- L. Qing, Y. Li, W. Tang, D. Zhang, Y. Han, and S. Zhao, "Dynamic adsorption of ions into like-charged nanopore: a dynamic density functional theory study." *Langmuir*, **35**, 4254 (2019).
- R. De Levie, "On porous electrodes in electrolyte solution-I,II,III." *Electrochimica Acta*, **8**, 751 (1963).
- R. De Levie, "On porous electrodes in electrolyte solutions-IV." *Electrochimica Acta*, **9**, 1231 (1964).
- R. De Levie, "Electrochemical response of porous and rough electrodes." *Advances in Electrochemistry and Electrochemical Engineering*, **6**, 329 (1967).
- J. Song and M. Z. Bazant, "Effects of nanoparticle geometry and size distribution on diffusion impedance of battery electrodes." *J. Electrochem. Soc.*, **160**, A15 (2012).
- J. Huang, Y. Gao, J. Luo, S. Wang, C. Li, S. Chen, and J. Zhang, "Review—impedance response of porous electrodes: theoretical framework, physical models and applications." *J. Electrochem. Soc.*, **167**, 166503 (2020).
- C. K. Li and J. Huang, "Impedance response of electrochemical interfaces: part I. Exact analytical expressions for ideally polarizable electrodes." *J. Electrochem. Soc.*, **167**, 166517 (2021).
- H. Wang and L. Pilon, "Intrinsic limitations of impedance measurements in determining electric double layer capacitances." *Electrochimica Acta*, **63**, 55 (2012).
- H. Wang and L. Pilon, "Reply to comments on 'Intrinsic limitations of impedance measurements in determining electric double layer capacitances' by H. Wang, L. Pilon [Electrochimica Acta 63 (2012) 55]." *Electrochimica Acta*, **76**, 529 (2012).
- H. Keiser, K. D. Beccu, and M. A. Gutjahr, "Abschätzung der porenstruktur poröser elektroden aus impedanzmessungen." *Electrochimica Acta*, **21**, 539 (1976).
- S. J. Cooper, A. Bertei, D. P. Finegan, and N. P. Brandon, "Simulated impedance of diffusion in porous media." *Electrochimica Acta*, **251**, 681 (2017).
- T. Aslyamov, K. Sinkov, and I. Akhatov, "Relation between charging times and storage properties of nanoporous supercapacitors." *Nanomaterials*, **12**, 587 (2022).
- J. Huang, S. Chen, and M. Eikerling, "Grand-canonical model of electrochemical double layers from a hybrid density-potential functional." *J. Chem. Theory and Computation*, **17**, 2417 (2021).
- P. Tarazona, J. A. Cuesta, and Y. Martínez-Ratón, "Density functional theories of hard particle systems." *Theory and Simulation of Hard-Sphere Fluids and Related Systems*, 247 (2008).

54. Y. Tang and J. Wu, "A density-functional theory for bulk and inhomogeneous Lennard-Jones fluids from the energy route." *J. Chem. Phys.*, **119**, 7388 (2003).
55. Z. Wang, L. Liu, and I. Neretnieks, "The weighted correlation approach for density functional theory: a study on the structure of the electric double layer." *J. Phys.: Condens. Matter*, **23**, 175002 (2011).
56. J. Wu, T. Jiang, D.-E. Jiang, Z. Jin, and D. Henderson, "A classical density functional theory for interfacial layering of ionic liquids." *Soft Matter*, **7**, 11222 (2011).
57. B. Medasani, Z. Ovanesyan, D. G. Thomas, M. L. Sushko, and M. Marucho, "Ionic asymmetry and solvent excluded volume effects on spherical electric double layers: a density functional approach." *J. Chem. Phys.*, **140**, 204510 (2014).
58. R. Roth, "Fundamental measure theory for hard-sphere mixtures: a review." *J. Phys.: Condens. Matter*, **22**, 063102 (2010).
59. A. Voukadinova, M. Valiskó, and D. Gillespie, "Assessing the accuracy of three classical density functional theories of the electrical double layer." *Physical Review E*, **98**, 012116 (2018).
60. L. Chacon, D. del Castillo-Negrete, and C. D. Hauck, "An asymptotic-preserving semi-Lagrangian algorithm for the time-dependent anisotropic heat transport equation." *J. Comput. Phys.*, **272**, 719 (2014).
61. J. Narski and M. Ottaviani, "Asymptotic preserving scheme for strongly anisotropic parabolic equations for arbitrary anisotropy direction." *Comput. Phys. Commun.*, **185**, 3189 (2014).
62. D. de Las Heras and M. Schmidt, "Full canonical information from grand-potential density-functional theory." *Phys. Rev. Lett.*, **113**, 238304 (2014).
63. F. Henrique, P. J. Zuk, and A. Gupta, "Impact of asymmetries in valences and diffusivities on the transport of a binary electrolyte in a charged cylindrical pore." *Electrochimica Acta*, **433**, 141220 (2022).
64. M.-M. Huang, Y. Jiang, P. Sasisanker, G. W. Driver, and H. Weingärtner, "Static relative dielectric permittivities of ionic liquids at 25 C." *J. Chem. Eng. Data*, **56**, 1494 (2011).
65. J. Hunger, A. Stoppa, S. Schrödle, G. Hefter, and R. Buchner, "Temperature dependence of the dielectric properties and dynamics of ionic liquids." *ChemPhysChem*, **10**, 723 (2009).
66. A. Noda, K. Hayamizu, and M. Watanabe, "Pulsed-gradient spin-echo 1h and 19f nmr ionic diffusion coefficient, viscosity, and ionic conductivity of non-chloroaluminate room-temperature ionic liquids." *J. Phys. Chem. B*, **105**, 4603 (2001).
67. J. Hoffmann and D. Gillespie, "Ion correlations in nanofluidic channels: effects of ion size, valence, and concentration on voltage- and pressure-driven currents." *Langmuir*, **29**, 1303 (2013).
68. A. Voukadinova and D. Gillespie, "Energetics of counterion adsorption in the electrical double layer." *J. Chem. Phys.*, **150**, 154706 (2019).
69. J. Terrones, P. J. Kiley, and J. A. Elliott, "Enhanced ordering reduces electric susceptibility of liquids confined to graphene slit pores." *Sci. Rep.*, **6**, 1 (2016).
70. S. Kondrat, P. Wu, R. Qiao, and A. A. Kornyshev, "Accelerating charging dynamics in subnanometre pores." *Nat. Mater.*, **13**, 387 (2014).
71. L. Qing, J. Lei, T. Zhao, G. Qiu, M. Ma, Z. Xu, and S. Zhao, "Effects of kinetic dielectric decrement on ion diffusion and capacitance in electrochemical systems." *Langmuir*, **36**, 4055 (2020).
72. D. Stopper, A. L. Thorneywork, R. P. A. Dullens, and R. Roth, "Bulk dynamics of Brownian hard disks: dynamical density functional theory vs experiments on two-dimensional colloidal hard spheres." *J. Chem. Phys.*, **148**, 104501 (2018).
73. T. L. Kirk, J. Evans, C. P. Please, and S. J. Chapman, "Modeling electrode heterogeneity in lithium-ion batteries: Unimodal and bimodal particle-size distributions." *SIAM Journal on Applied Mathematics*, **82**, 625 (2022).
74. M. K. Borg, D. A. Lockerby, and J. M. Reese, "A hybrid molecular-continuum method for unsteady compressible multiscale flows." *J. Fluid Mech.*, **768**, 388 (2015).
75. M. G. Knepley, D. A. Karpeev, S. Davidovits, R. S. Eisenberg, and D. Gillespie, "An efficient algorithm for classical density functional theory in three dimensions: ionic solutions." *J. Chem. Phys.*, **132**, 124101 (2010).
76. H.-Y. Yu, Z. Jabeen, D. M. Eckmann, P. S. Ayyaswamy, and R. Radhakrishnan, "Microstructure of flow-driven suspension of hardspheres in cylindrical confinement: a dynamical density functional theory and Monte Carlo study." *Langmuir*, **33**, 11332 (2017).
77. J. F. Lutsko and J. Lam, "Classical density functional theory, unconstrained crystallization, and polymorphic behavior." *Physical Review E*, **98**, 012604 (2018).
78. M. Valiskó, T. Kristóf, D. Gillespie, and D. Boda, "A systematic monte carlo simulation study of the primitive model planar electrical double layer over an extended range of concentrations, electrode charges, cation diameters and valences." *AIP Adv.*, **8**, 025320 (2018).
79. J. A. Carrillo, A. Chertock, and Y. Huang, "A finite-volume method for nonlinear nonlocal equations with a gradient flow structure." *Communications in Computational Physics*, **17**, 233 (2015).
80. A. Russo, S. P. Perez, M. A. Durán-Olivencia, P. Yatsyshin, J. A. Carrillo, and S. Kalliadasis, "A finite-volume method for fluctuating dynamical density functional theory." *J. Comput. Phys.*, **428**, 109796 (2020).